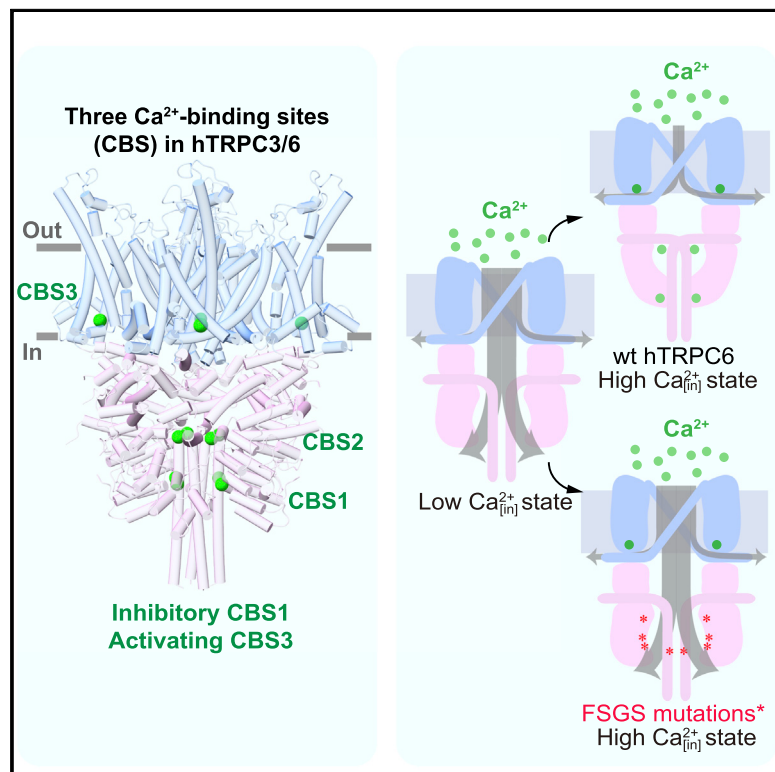


Structural mechanism of human TRPC3 and TRPC6 channel regulation by their intracellular calcium-binding sites

Graphical abstract



Authors

Wenjun Guo, Qinglin Tang, Miao Wei,
Yunlu Kang, Jing-Xiang Wu, Lei Chen

Correspondence

chenlei2016@pku.edu.cn

In brief

Guo et al. identified three intracellular calcium-binding sites (CBS) in the hTRPC3/6 channel: CBS1 is inhibitory and CBS3 is activating. Gain-of-function mutations of hTRPC6 impair the inhibitory CBS1 but retain the activating CBS3, resulting in the positive feedback of calcium signals in podocytes and, finally, leading to the disease FSGS.

Highlights

- Structures of hTRPC3/6 reveal three intracellular calcium-binding sites (CBS1–3)
- The interplay between inhibitory CBS1 and activating CBS3 regulates channel activity
- The gain-of-function FSGS mutations impair the inhibitory function of CBS1 in hTRPC6
- Inhibitors BTDM and SAR7334 stabilize hTRPC6 in distinct non-conductive states



Article

Structural mechanism of human TRPC3 and TRPC6 channel regulation by their intracellular calcium-binding sites

Wenjun Guo,¹ Qinglin Tang,¹ Miao Wei,¹ Yunlu Kang,¹ Jing-Xiang Wu,^{1,2,3} and Lei Chen^{1,2,3,4,*}

¹State Key Laboratory of Membrane Biology, College of Future Technology Institute of Molecular Medicine, Beijing Key Laboratory of Cardiometabolic Molecular Medicine, Peking University, Beijing 100871, China

²Peking-Tsinghua Center for Life Sciences, Peking University, Beijing 100871, China

³Academy for Advanced Interdisciplinary Studies, Peking University, Beijing 100871, China

⁴Lead contact

*Correspondence: chenlei2016@pku.edu.cn

<https://doi.org/10.1016/j.neuron.2021.12.023>

SUMMARY

TRPC3 and TRPC6 channels are calcium-permeable non-selective cation channels that are involved in many physiological processes. The gain-of-function (GOF) mutations of *TRPC6* lead to familial focal segmental glomerulosclerosis (FSGS) in humans, but their pathogenic mechanism remains elusive. Here, we report the cryo-EM structures of human TRPC3 in both high-calcium and low-calcium conditions. Based on these structures and accompanying electrophysiological studies, we identified both inhibitory and activating calcium-binding sites in TRPC3 that couple intracellular calcium concentrations to the basal channel activity. These calcium sensors are also structurally and functionally conserved in TRPC6. We uncovered that the GOF mutations of *TRPC6* activate the channel by allosterically abolishing the inhibitory effects of intracellular calcium. Furthermore, structures of human TRPC6 in complex with two chemically distinct inhibitors bound at different ligand-binding pockets reveal different conformations of the transmembrane domain, providing templates for further structure-based drug design targeting TRPC6-related diseases such as FSGS.

INTRODUCTION

Canonical transient receptor potential (TRPC) channels are the closest mammalian homologs of the *Drosophila* TRP channel (Wes et al., 1995; Zhu et al., 1995). They are calcium-permeable non-selective cation channels (Feng, 2017). Receptor activation enhances the activities of phospholipase C (PLC), which hydrolyze PIP₂ to produce the second messenger diacylglycerol (DAG). DAG activates TRPC channels. According to the sequence homology and electrophysiological property, TRPC3, TRPC6, and TRPC7 cluster as one subfamily, and TRPC1, TRPC4, and TRPC5 form another subfamily (Guo and Chen, 2019). TRPC3/6/7 channels participate in a range of neurological processes. TRPC3 is involved in neurotrophin BDNF signals (Li et al., 1999), synaptic transmission, and motor coordination (Hartmann et al., 2008; Hartmann and Konnerth, 2015). TRPC6 channels promote cerebellar granule neuron survival (Jia et al., 2007) and play a critical role in the formation of excitatory synapses (Zhou et al., 2008). Additionally, these channels are also involved in many physiological processes and pathological disease conditions (Abramowitz and Birnbaumer, 2009), including pathologic cardiac hypertrophy, regulation of myogenic tone

and blood pressure, hypoxic pulmonary vasoconstriction, regulation of the endothelial barrier function, traumatic brain injury, arteriosclerosis, cancer treatment, diabetes, and kidney function (Chen et al., 2020). Notably, the autosomal dominant mutations of the human *TRPC6* gene lead to familial focal segmental glomerulosclerosis (FSGS) (Reiser et al., 2005; Winn et al., 2005) with symptoms of proteinuria and progressive chronic kidney disease (Pollak, 2014). Most of the *TRPC6* mutations associated with FSGS are gain-of-function (GOF) mutations, which cause the disease probably by enhancing the channel activity and ultimately leading to calcium overload of kidney podocytes (Pollak, 2014). Therefore, pharmacological inhibition of the TRPC6 channel provides a promising treatment for FSGS caused by GOF *TRPC6* mutations. Moreover, the activities of TRPC3/6/7 channels are regulated by calcium. It is reported that the TRPC3 and TRPC7 currents are modulated by calcium (Kamouchi et al., 1999; Lintschinger et al., 2000; Shi et al., 2004; Zhang et al., 2001; Zitt et al., 1997). It is also proposed that calmodulin (Boulay, 2002) or CaMKII (Shi et al., 2004) mediates the calcium regulation of the TRPC6 channel. However, the structural mechanism of calcium regulation and its connections with FSGS mutations of TRPC6 are largely unknown.



Recent studies have revealed the structures of several TRPC homo-tetramers, including TRPC3, TRPC4, TRPC5, and TRPC6 (Guo and Chen, 2019). These structures show the overall two-layer architecture, namely, the transmembrane domain (TMD) layer and the intracellular cytosolic domain (ICD) layer. The TMD is formed by the ion-channel pore and the voltage-sensor-like domain (VSLD) in a domain-swapped fashion. A high-affinity inhibitor, (2-(benzo[d][1,3]dioxol-5-ylamino)thiazol-4-yl)((3S,5R)-3,5-dimethylpiperidin-1-yl)methanone (BTDM), wedges between the pore and VSLD to inhibit TRPC6 opening (Tang et al., 2018), and another inhibitor, AM-1473, binds to the pocket formed by S1–S4 and the TRP helix to maintain the TRPC6 channel in a closed state (Bai et al., 2020). The ICD is formed by an N-terminal ankyrin repeat domain (ARD), linker helices domain (LHD), horizontal C-terminal helix 1 (CH1), and vertical C-terminal helix 2 (CH2) (Guo and Chen, 2019). These domains from four structurally symmetric subunits assemble into an inverted bell-shaped ICD that caps below the TMD (Guo and Chen, 2019). In some of the resolved TRPC structures, ICDs are tightly sealed to form a dome that is hardly permeable to cations, whereas in other structures, ICDs are loosely packed to allow cation permeation (Guo and Chen, 2019). Interestingly, most of the GOF mutations of hTRPC6 that cause FSGS are located in the ICD. However, how these mutations cause over-activation of hTRPC6 and how ICD regulates the function of the TRPC channel at the molecular level remain enigmatic. To answer these fundamental questions, we conducted structural and electrophysiological studies on human TRPC3 (hTRPC3) and human TRPC6 (hTRPC6) channels.

RESULTS

Structures of hTRPC3 in high-calcium and low-calcium conditions

The hTRPC3 channel has low but detectable basal activity in the absence of exogenous DAG (Nikolaev et al., 2019). We found both the inward and the outward basal currents of the hTRPC3 were reversibly inhibited by intracellular calcium in a dose-dependent manner (Figures 1A–1C, S1A, and S1B), similar to the mTRPC7 channel (Shi et al., 2004). In addition, over-expression of wild-type (WT) calmodulin or its calcium-binding site mutant (D21A+D57A+D94A+D130A, CaM-4DA) (Shi et al., 2004) did not affect calcium inhibition (Figures S1C–S1E). We further found that calcium markedly enhanced the thermostability of purified hTRPC3 protein or cell lysates containing unpurified hTRPC3 protein (Figures 1D, 1E, and S1F–S1H) (Hattori et al., 2012). These findings collectively suggest that calcium inhibits the basal currents of hTRPC3, possibly by directly binding to hTRPC3.

To identify the calcium-binding sites on hTRPC3, we reconstituted purified hTRPC3 protein into nanodiscs and prepared cryo-EM samples in both high-calcium (1 mM calcium) and low-calcium (1 mM EDTA and 1 mM EGTA) conditions for single-particle analysis (Figures S2 and S3). The final reconstructions of hTRPC3 in high-calcium (hTRPC3_{high-calcium}) and low-calcium (hTRPC3_{low-calcium}) conditions reached 2.7- and 3.1-Å resolutions, respectively (Figures 1F–1K, S2, and S3; Table S1). In hTRPC3_{high-calcium}, the ICD of hTRPC3 shows a tightly packed structure (Figures 1F–1H), which resembles our previous 4.4-Å

hTRPC3 structure (PDB: 5ZBG), prepared as nanodiscs in Tris-buffered saline (TBS) (Tang et al., 2018). Retrospectively, we found that TBS buffer contained around 4 µM calcium, which is high enough to completely inhibit the hTRPC3 channel (Figures 1A–1C), suggesting that calcium was bound in ICD of our previous hTRPC3 structure (Tang et al., 2018). Strikingly, the ICD of hTRPC3_{low-calcium} shows a loosely packed structure (Figures 1I–1K), which resembles the published 3.3-Å hTRPC3 structure in digitonin detergent supplemented with 1 mM EDTA (PDB: 6CUD) (Fan et al., 2018). These results comprehensively reveal that the large structural differences of ICD between the published hTRPC3 structures (Fan et al., 2018; Guo and Chen, 2019; Tang et al., 2018) are mainly due to the binding of calcium ions.

Calcium-binding sites in hTRPC3

The high-resolution structures in both high-calcium and low-calcium conditions allowed us to locate three distinct calcium-binding sites (CBS1–3) (Figures 2 and S4) using two structural criteria: (1) there should be at least two negatively charged residues for stably chelating divalent calcium ion in the CBS, and (2) the occupancies of putative calcium ion should change accordingly between high-calcium and low-calcium conditions. Because the hTRPC3 channel is a homo-tetramer, one hTRPC3 channel has four identical copies of CBS1–3 and thus 12 CBS in total.

CBS1 is situated between ankyrin repeat 2 (AR2) and CH2 (Figures 2A and 2B). This region is highly negatively charged (Figure S4A). The ion is coordinated by the main-chain carbonyl group and the side-chain carboxyl group of E73 that is located on AR2 and the side-chain carboxyl group of D798 located on CH2 (Figure 2B). In hTRPC3_{low-calcium}, this CBS is disrupted due to the dissociation of ARD and CH2 (Figures S4D–S4G). To reveal the function of CBS1, we mutated D798 on CH2 into alanine to reduce the binding of calcium in CBS1 (Figure S5). We found that the D798A mutation largely abolished the inhibition of hTRPC3 by intracellular calcium (Figures 2E and S5A), suggesting that the CBS1 is inhibitory. Consistent with this, the thermostability of D798A is not markedly enhanced by calcium anymore (Figures 2F and S5B). Residues of CBS1 are absolutely conserved during evolution, from the ancient *Drosophila* TRP channel to human TRPC channels, suggesting its functional importance (Figure 2B).

CBS2 is located in a negatively charged region at the top of CH2 (Figure S4B) and is formed by the side chain of E791, the main chain of E786 of one subunit, and the side chain of E789 of the adjacent subunit (Figures 2A and 2C). CBS2 is disrupted in hTRPC3_{low-calcium} (Figures S4H–S4K). The residues of CBS2 are conserved in TRPC3/6/7. We found that the currents of E789A mutant retain robust calcium inhibition (Figures 2E and S5C), and its thermostability in low-calcium conditions is moderately enhanced compared with the WT channel (Figures 2F and S5D), suggesting a minor role of CBS2 for calcium regulation.

CBS3 is located within the VSLD of TMD (Figures 2A and 2D). The calcium ion is coordinated by the side chains of E440, E443 on S2, and N458 on S3 (Figure 2D) and sits in a negatively charged environment (Figure S4C). In the map of hTRPC3_{low-calcium}, this density is missing, confirming the identity of calcium ions (Figures S4L–S4O). Residues of CBS3 are conserved in TRPC channels except for TRPC1 (Figure 2D).

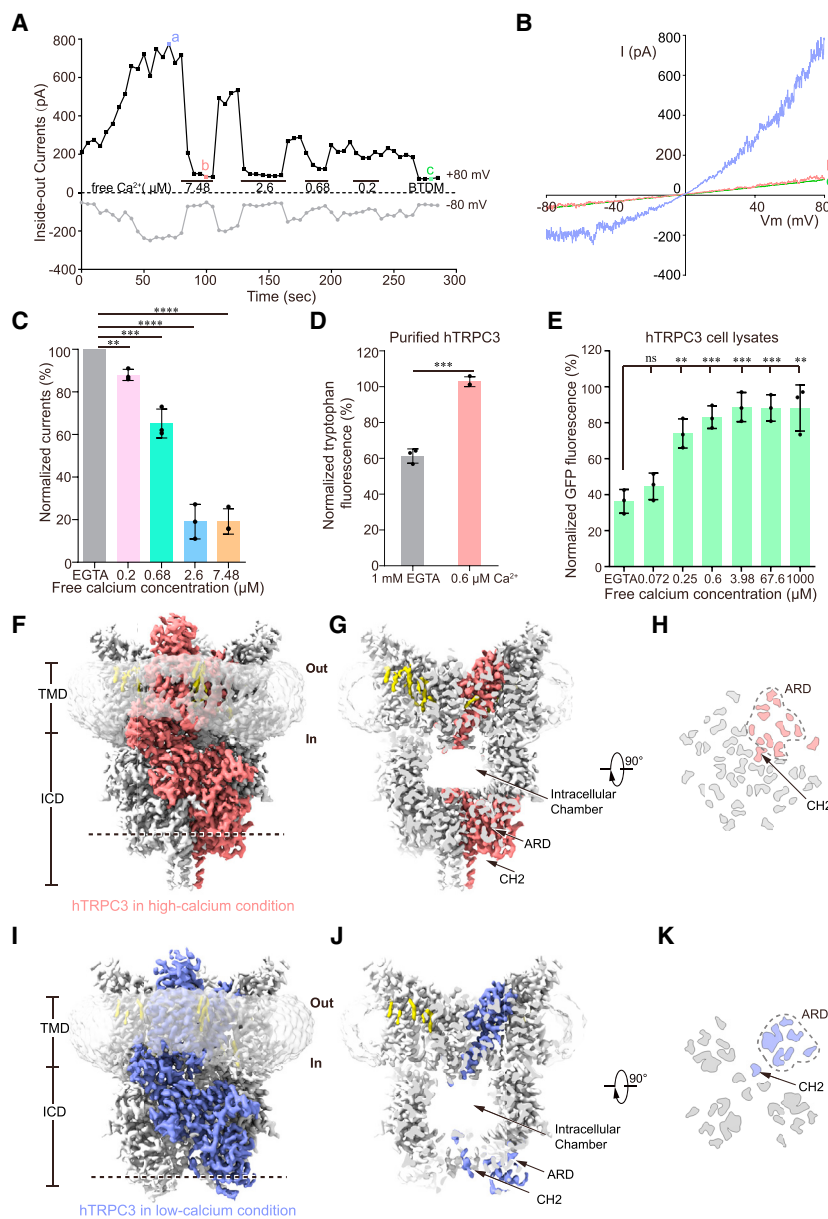


Figure 1. Structures of hTRPC3 in high-calcium and low-calcium states

(A) Inside-out currents of hTRPC3 in the presence of calcium. Currents at -80 and $+80$ mV were presented. Calcium concentrations were indicated by horizontal bars.

(B) Ramped I-V curves of hTRPC3 at time points shown in (A).

(C) Effects of intracellular calcium on hTRPC3 currents in the inside-out mode. Currents were normalized to the low-calcium bath solution. The data were shown as the mean \pm SD (3 independent patches). Two-tailed Student's t test, ** $p < 0.01$, *** $p < 0.001$, **** $p < 0.0001$.

(D) Thermostability of purified hTRPC3 protein in the presence of low-calcium or $0.6 \mu\text{M}$ free calcium. The tryptophan fluorescence of hTRPC3 tetramer after heating was normalized to that without heating. $n = 3$ biological replicates. The data were shown as the mean \pm SD. Two-tailed Student's t test, *** $p < 0.001$.

(E) The effect of calcium on the thermostability of hTRPC3 in cell lysates. The GFP fluorescence of hTRPC3 tetramer peak after heating was normalized to that without heating. $n = 3$ biological replicates. The data were shown as the mean \pm SD. Two-tailed Student's t test, ** $p < 0.01$, *** $p < 0.001$.

(F) Side view of the cryo-EM map of hTRPC3 in high-calcium condition (hTRPC3_{high-calcium}). One subunit is in pink and the other subunits are in gray. Density corresponding to nanodiscs is shown in gray with transparency. Lipids are in yellow. TMD, transmembrane domain; ICD, intracellular domain.

(G) Sliced view of TRPC3_{high-calcium}. ARD, ankyrin repeat domain; CH, C-terminal helix.

(H) Bottom view of the cross-section of the ICD at the position marked as a dashed line in (F). Each subunit is colored the same as in (F). The ARD of one subunit is circled by a dashed line.

(I) Side view of the cryo-EM map of hTRPC3 in low-calcium condition (hTRPC3_{low-calcium}). One subunit is in blue, and the remaining part of density is colored the same as in (F).

(J) Sliced view of hTRPC3_{low-calcium}.

(K) Bottom view of the cross-section of the ICD at the same position as (F) and marked as a dashed line in (I).

See also Figures S1, S2, and S3 and Table S1.

CBS3 was previously proposed as a cation-binding site for TRPC4 (Duan et al., 2018; Vinayagam et al., 2020), TRPC5 (Duan et al., 2019; Song et al., 2021), and an activating calcium-ion-binding site for TRPM (Autzen et al., 2018; Huang et al., 2018; Wang et al., 2018; Zhang et al., 2018). The mutation E893A in nvTRPM2 abolishes calcium activation (Zhang et al., 2018). To explore the function of CBS3 in hTRPC3, we generated an E440A mutant (corresponding to E893A of nvTRPM2) to weaken calcium binding in CBS3. The thermostability of E440A is similar to WT hTRPC3 (Figures 2F and S5F), suggesting that CBS3 is not involved in the calcium-dependent enhancement of thermostability. Although we found that the E440A mutant is still inhibited by calcium (Figures 2E, S5E, and S5L), CBS3 might play an activating role in hTRPC3 based on its structure and

sequence similarity to TRPM channels. This is confirmed by studying the GOF mutants in hTRPC3 as shown later.

We found that the CBS1–3 triple mutants (E440A, E789A, and D798A) of hTRPC3 can be activated by 1-oleoyl-2-acetyl-sn-glycerol (OAG), a soluble DAG analog (Figures S5G and S5H), suggesting that these mutations do not affect the activation of DAG, which likely binds in the TMD due to its hydrophobic nature (Song et al., 2021). However, we found that although the extracellular calcium robustly inhibits the whole-cell currents of WT hTRPC3 at holding potential of -60 mV, deflecting the holding potential to $+60$ mV abolishes such inhibition (Figures 2G, S5I, and S5J), indicating that the extracellular calcium inhibition of hTRPC3 is mediated by calcium influx and the subsequent effect of intracellular calcium. More importantly, we found that

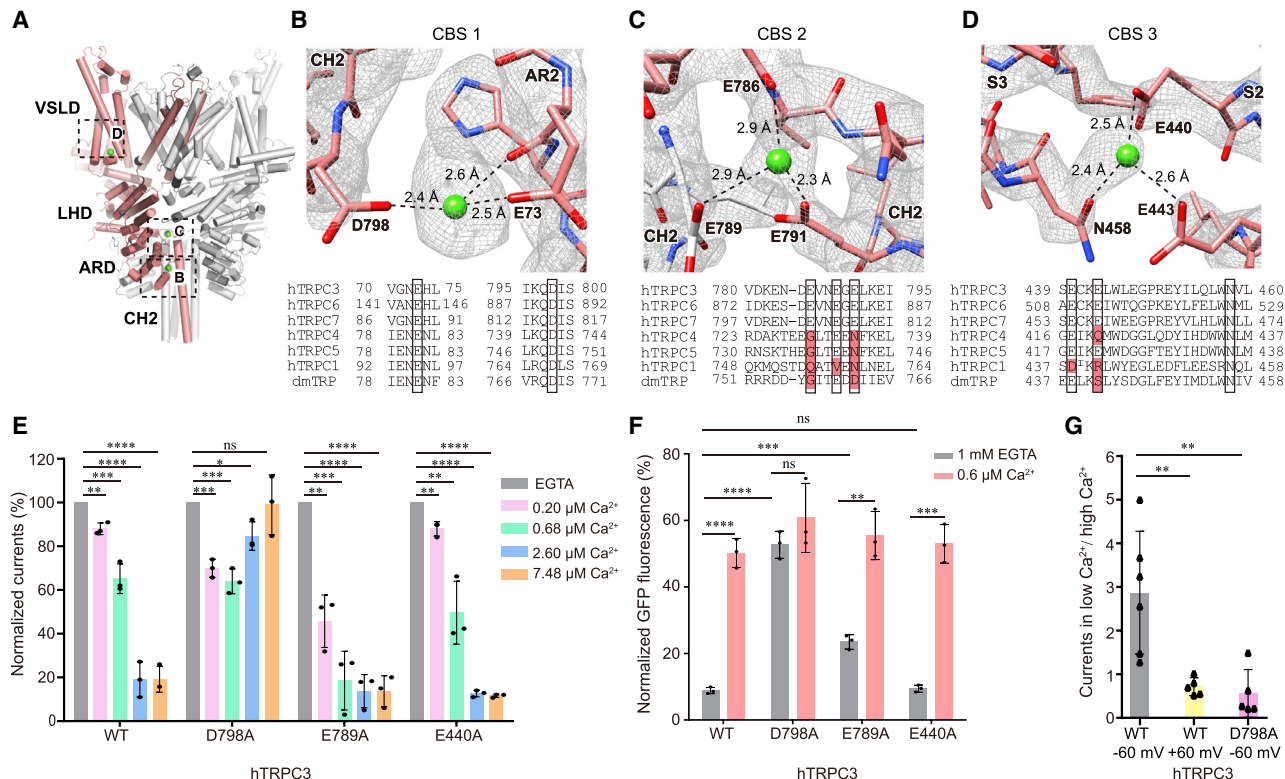


Figure 2. Calcium-binding sites of hTRPC3

(A) Overview of the three calcium-binding sites (CBS1–3) of hTRPC3. The cartoon model of hTRPC3 in cylinders and colored the same as in Figure 1F. The calcium ions are shown as green spheres. VSLD, voltage-sensor-like domain; LHD, linker helices domain; ARD, ankyrin repeat domain.

(B–D) Close-up view of the CBS1–3 boxed in (A). Densities of ions and surrounding amino acids are contoured at 4.8σ and shown as gray meshes. Sequence alignments between human TRPCs and *Drosophila* TRP (dmTRP) are shown below. Residues that interact with ions are boxed. Non-conserved residues are colored in red.

(E) The effects of intracellular calcium on the currents of various hTRPC3 constructs measured in the inside-out mode. $n = 3$ independent patches and the data were shown as the mean \pm SD. Two-tailed Student's t test, * $p < 0.05$, ** $p < 0.01$, *** $p < 0.001$, **** $p < 0.0001$.

(F) Effect of calcium on the thermostability of WT hTRPC3 and its mutants in cell lysates. $n = 3$ biological replicates. The data were shown as the mean \pm SD. Two-tailed Student's t test, ** $p < 0.01$, *** $p < 0.001$, **** $p < 0.0001$.

(G) The ratio of OAG-evoked whole-cell currents in low-calcium solution over high-calcium solution for WT hTRPC3 and CBS1 mutant D798A. Holding potentials are indicated below. Two-tailed Student's t test, ** $p < 0.01$.

See also Figures S4 and S5.

CBS1 mutation D798A impairs extracellular calcium inhibition of hTRPC3 at a holding potential of -60 mV (Figures 2G and S5K), suggesting that CBS1 mediates the inhibition of DAG-evoked currents by extracellular calcium.

Conformational changes upon calcium unbinding allow ion permeation through ICD

Structural comparison of hTRPC3_{high-calcium} and hTRPC3_{low-calcium} reveals that both the ICD layer and the TMD layer show conformational changes upon calcium dissociation (Figure 3; Video S1).

In hTRPC3_{high-calcium}, the ICD shows a tightly packed conformation in which the ARD (AR1–AR4) is near the CH2 helices (Figures 3A–3C) and multiple inter-domain interactions stabilize the ARD-CH2 interface (Tang et al., 2018). Because both CBS1 and CBS2 are formed by opposing negatively charged residues (Figures 2B and 2C), the binding of positively charged divalent calcium ions at these sites would neutralize the repulsive negative charges and, in turn, would result in a compact structure, which is relatively more thermostable (Figure 1D). As ICD caps below the pore of the TRPC channel, extracellular cations would initially flow into the intracellular chamber inside the ICD through the transmembrane pore and then into the cytosol. Tunnel calculation shows that in the tightly packed conformation, the ICD itself is largely sealed, and ion permeability through ICD is low. Ions inside the intracellular chamber can only flow into the cytosol through the lateral opening (Tunnel A) sandwiched between ICD and TMD (Figures 3D and 3F). Electrostatic surface calculation showed several positively charged patches along Tunnel A, suggesting a high-energy barrier for cation permeation (Figure 3G). This is in agreement with the small BTDM-sensitive residual currents in the high-calcium condition (Figures 1A and S1). In hTRPC3_{low-calcium}, negatively charged side chains of CBS1 and CBS2 repel each other, which, in turn, causes the dissociation between AR2 and CH2 and the opening of ICD

tive charges and, in turn, would result in a compact structure, which is relatively more thermostable (Figure 1D). As ICD caps below the pore of the TRPC channel, extracellular cations would initially flow into the intracellular chamber inside the ICD through the transmembrane pore and then into the cytosol. Tunnel calculation shows that in the tightly packed conformation, the ICD itself is largely sealed, and ion permeability through ICD is low. Ions inside the intracellular chamber can only flow into the cytosol through the lateral opening (Tunnel A) sandwiched between ICD and TMD (Figures 3D and 3F). Electrostatic surface calculation showed several positively charged patches along Tunnel A, suggesting a high-energy barrier for cation permeation (Figure 3G). This is in agreement with the small BTDM-sensitive residual currents in the high-calcium condition (Figures 1A and S1). In hTRPC3_{low-calcium}, negatively charged side chains of CBS1 and CBS2 repel each other, which, in turn, causes the dissociation between AR2 and CH2 and the opening of ICD

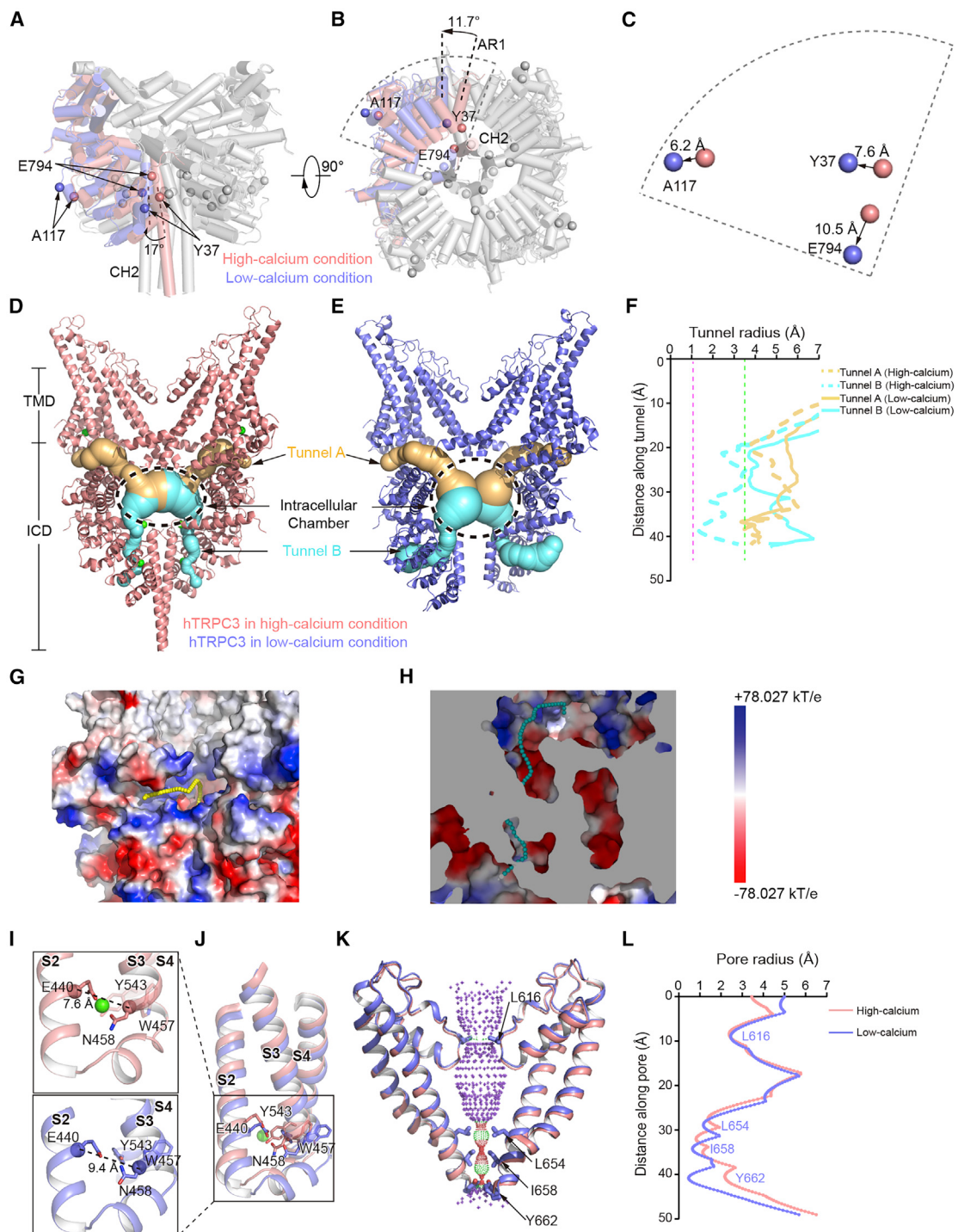


Figure 3. Conformational changes of hTRPC3 between high-calcium and low-calcium states

(A) ICD structures of hTRPC3_{high-calcium} (pink) and hTRPC3_{low-calcium} (blue) are overlaid by aligning their TMD. Only one subunit is colored, and the other subunits are in gray. C_α atoms of Y37 on AR1, A117 on the AR3-AR4 loop, and E794 on CH2 are used as marker atoms and shown as spheres. The angle between CH2 at the two states is measured.

(B) Bottom view of hTRPC3 ICD. The angle between AR1 helices in the two states is shown.

(C) Close-up view of the movements of marker atoms shown in (B).

(D) Putative ion permeation pathways between the chamber of ICD and cytosol of hTRPC3_{high-calcium} calculated by Caver. Two diagonal-arranged subunits and associated tunnels are shown for clarity.

(legend continued on next page)

(Figures 3A–3C; Video S1). ARD rotates counterclockwise for 11.7 degrees (Figure 3B). In the absence of stabilizing interactions with ARD, the four helical bundles of CH2 rotate for 17 degrees concomitantly (Figure 3A) and is more flexible, as manifested by poor local resolution (Figures S3G and S3H). These motions collectively lead to the loosely packed structure of ICD (Figure 3E), which is less stable compared with the tightly packed high-calcium-state structure (Figure 1D). Notably, in the loosely packed state, additional ion permeation pathways (e.g., Tunnel B) inside ICD dilate largely enough to allow the flow of cations, such as hydrated calcium (Barger and Dillon, 2016) (Figures 3E and 3F). Electrostatic surface calculation showed several negatively charged patches in Tunnel B, which might facilitate cation permeation (Figure 3H). This newly formed Tunnel B is in parallel to Tunnel A, and both Tunnel A and Tunnel B are in series to the transmembrane pore. As a result, the electrical resistance from the intracellular chamber to the cytosol is largely decreased, which likely account for the markedly enhanced hTRPC3 basal currents at low-calcium conditions (Figures 1A–1C and S1).

In the TMD, the binding of calcium to CBS3 brings S2 and S3 closer to each other (Figures 3I and 3J). The C α atom distance between calcium-chelating residues E440 on S2 and N458 on S3 shrinks from 9.4 to 7.6 Å (Figure 3I). The movements of S2 and S3 lead to the positional displacement of the side chains of W457 on S3 and Y543 on S4. These changes are further conveyed to the adjacent S5 and S6 pore helices and result in a small but noticeable dilation of the gate (Figures 3K and 3L). Nevertheless, the ion channel pore in both high-calcium and low-calcium states remain closed (Figures 3K and 3L) in agreement with the small basal currents due to the low open probability of TRPC3 (Nikolaev et al., 2019).

The regulation of hTRPC6 basal activity by intracellular calcium

To explore the effect of intracellular calcium on hTRPC6, we measured its basal currents and thermostability of hTRPC6 at different calcium concentrations (Figures 4 and S6). We found that the thermostability of hTRPC6 is enhanced by calcium (Figures 4C, S6A, and S6B), similar to hTRPC3 (Figure 1). However, 200 nM calcium activates hTRPC6, whereas 7.48 μM calcium evokes peak currents with inactivation (Figures 4A and S6C). The steady-state currents of hTRPC6 showed bell-shaped regulation by intracellular calcium (Figure 4I), as previously reported (Shi et al., 2004). To elucidate the mechanism of calcium binding and regulation of the hTRPC6 channel, we performed structural studies of hTRPC6 in the presence of 1 mM CaCl₂ using a functional truncated hTRPC6 construct (72–904 aa) (Tang et al.,

2018). Because the TMD of hTRPC6 is unstable in the absence of ligands, the purified protein was reconstituted into nanodiscs and supplemented with a high-affinity inhibitor BTDM (Tang et al., 2018). We resolved the cryo-EM structure of hTRPC6 in a high-calcium state at a resolution of 2.9 Å (Figures 4D, 4E, and S7; Table S1). The overall structure is similar to our 3.8-Å structure of hTRPC6 published previously (Tang et al., 2018) but with markedly enhanced details. We observed calcium densities at CBS1–3 of this map (Figures 4F–4H). Mutagenesis results showed that CBS3 mutant E509A (as E440 of hTRPC3) showed no activation by calcium but a concentration-dependent inhibition by calcium, suggesting that CBS3 plays an activating role in hTRPC6 (Figures 4I, S6D, and S6M). In contrast, CBS1 mutant D890A (as D798 of hTRPC3) showed monophasic activation instead of the bell-shaped regulation by calcium (Figures 4I and S6E), suggesting that CBS1 plays an inhibitory role in hTRPC6. CBS2 mutant E881 showed tiny currents that did not allow further characterization. Similar to hTRPC3, the D890A mutation (CBS1) abolished the calcium regulation of hTRPC6 protein thermostability, whereas the E881A mutation (CBS2) imparts a mild effect and E509A (CBS3) has no effect (Figures 4J and S6F–S6H). The CBS1–3 triple mutant (E509A, D890A, and E881A) of hTRPC6 is robustly activated by OAG (Figures S6I and S6J), suggesting the preserved DAG-activation. The OAG-activated currents of hTRPC6 are also inhibited by extracellular calcium, and CBS1 mutation (D890A) abolished such inhibition (Figures 4K, S6K, and S6L).

Mechanism of GOF FSGS mutations of hTRPC6

Mapping of GOF FSGS mutations (Gigante et al., 2011; Riehle et al., 2016) onto the hTRPC6 structure revealed that these mutations cluster within the ICD (Figures 5A–5C) and probably affect the stability of ARD-CH2 interfaces, which are important for both calcium inhibition and protein thermostability. Indeed, the thermostability of these FSGS mutants was not enhanced by 1 μM calcium anymore (Figure 5D) and the basal currents of all the FSGS mutants were markedly increased by intracellular calcium in a monophasic manner (Figures 5E and S8A–S8H), suggesting that they share common defects of the inhibitory function of CBS1, even though residues of CBS1 were unaltered in these mutants. To study the mechanism of hTRPC6 FSGS mutations, we focused on the R895C mutant located on CH2 (Figure 5F). R895 interacts with E897 on CH2 and E147 on ARD of the adjacent subunit (Figure 5F). The R895C mutation probably destabilizes the ARD-CH2 interface and thus allosterically weakens calcium binding at CBS1 and impairs the inhibitory function of CBS1. Indeed, the currents of R895C of hTRPC6 show strong activation in response to calcium (Figures 5E and

(E) Putative ion permeation pathways between the chamber of ICD and cytosol of hTRPC3_{low-calcium} calculated by Caver.

(F) Calculated tunnel radius shown in (D) and (E). The radius of dehydrated calcium ion (1.0 Å) is indicated as a pink dashed line and the radius of fully hydrated calcium ion (3.34 Å) is indicated as a green dashed line.

(G) The electrostatic potential along Tunnel A (center is shown as yellow dots) in hTRPC3_{low-calcium} calculated by Pymol.

(H) The electrostatic potential along Tunnel B (center is shown as cyan dots) in hTRPC3_{low-calcium}.

(I) Conformational change of VSLD upon calcium binding. The helices are shown in pink for the high-calcium state and blue for the low-calcium state. The C α atoms of E440 and N458 are shown as spheres, and the calcium ion is shown as a green sphere.

(J) Structural comparison of the VSLD in high-calcium and low-calcium states by aligning the S5 and S6.

(K) Structure of channel pore in high-calcium (pink) and low-calcium (blue) states.

(L) Pore profile of hTRPC3_{high-calcium} and hTRPC3_{low-calcium} calculated by HOLE.

See also Video S1.

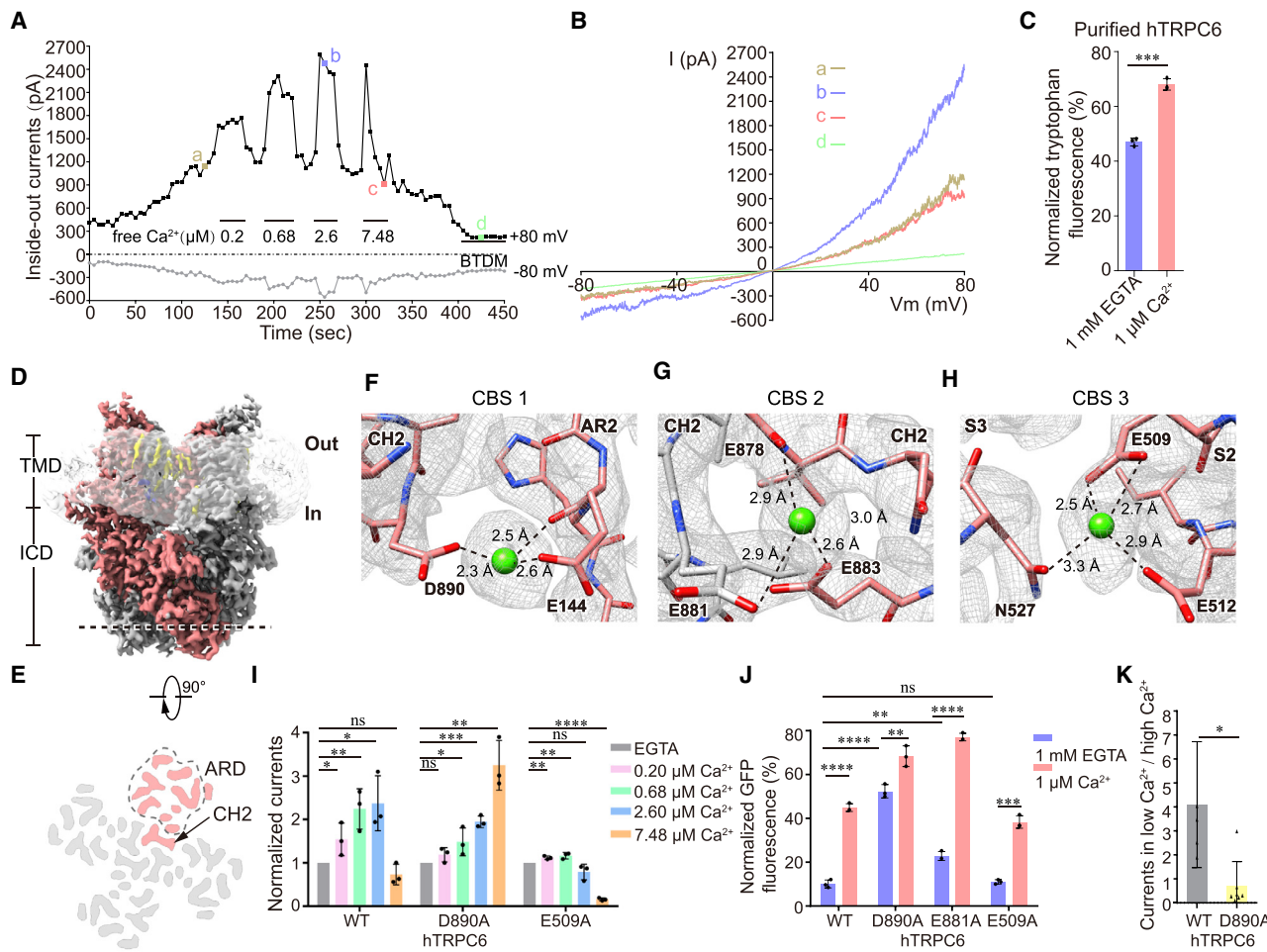


Figure 4. Structure of hTRPC6 in the high-calcium state

(A) The effect of calcium on hTRPC6 currents measured in the inside-out mode. Free calcium concentrations were indicated by horizontal bars.

(B) Ramped I-V curves of hTRPC6 at different time points as indicated in (A).

(C) Effect of calcium on the thermostability of purified hTRPC6 channel measured by tryptophan fluorescence. $n = 3$ biological replicates. The data are shown as the mean \pm SD. Two-tailed Student's t test, *** $p < 0.001$.

(D) Side view of hTRPC6_{high-Ca²⁺}, colored the same as Figure 1F.

(E) Bottom view of the cross-section of the ICD at the position marked by the dashed line in (D).

(F-H) Close-up view of the CBS1-3 of hTRPC6_{high-Ca²⁺}. The densities of ions and related amino acids are contoured at 5 σ for CBS1, and 3 σ for CBS2 and CBS3, and are presented as gray meshes.

(I) The effects of intracellular calcium on hTRPC6 currents measured in the inside-out mode. Currents were normalized to the low-calcium bath solution. The data are shown as the mean \pm SD ($n = 3$ three independent patches). One-tailed Student's t test, * $p < 0.05$, ** $p < 0.01$, *** $p < 0.001$, **** $p < 0.0001$.

(J) Effect of calcium on the thermostability of WT hTRPC6 and its mutants in cell lysates. $n = 3$ biological replicates. The data are shown as the mean \pm SD. Two-tailed Student's t test, ** $p < 0.01$, *** $p < 0.001$, **** $p < 0.0001$.

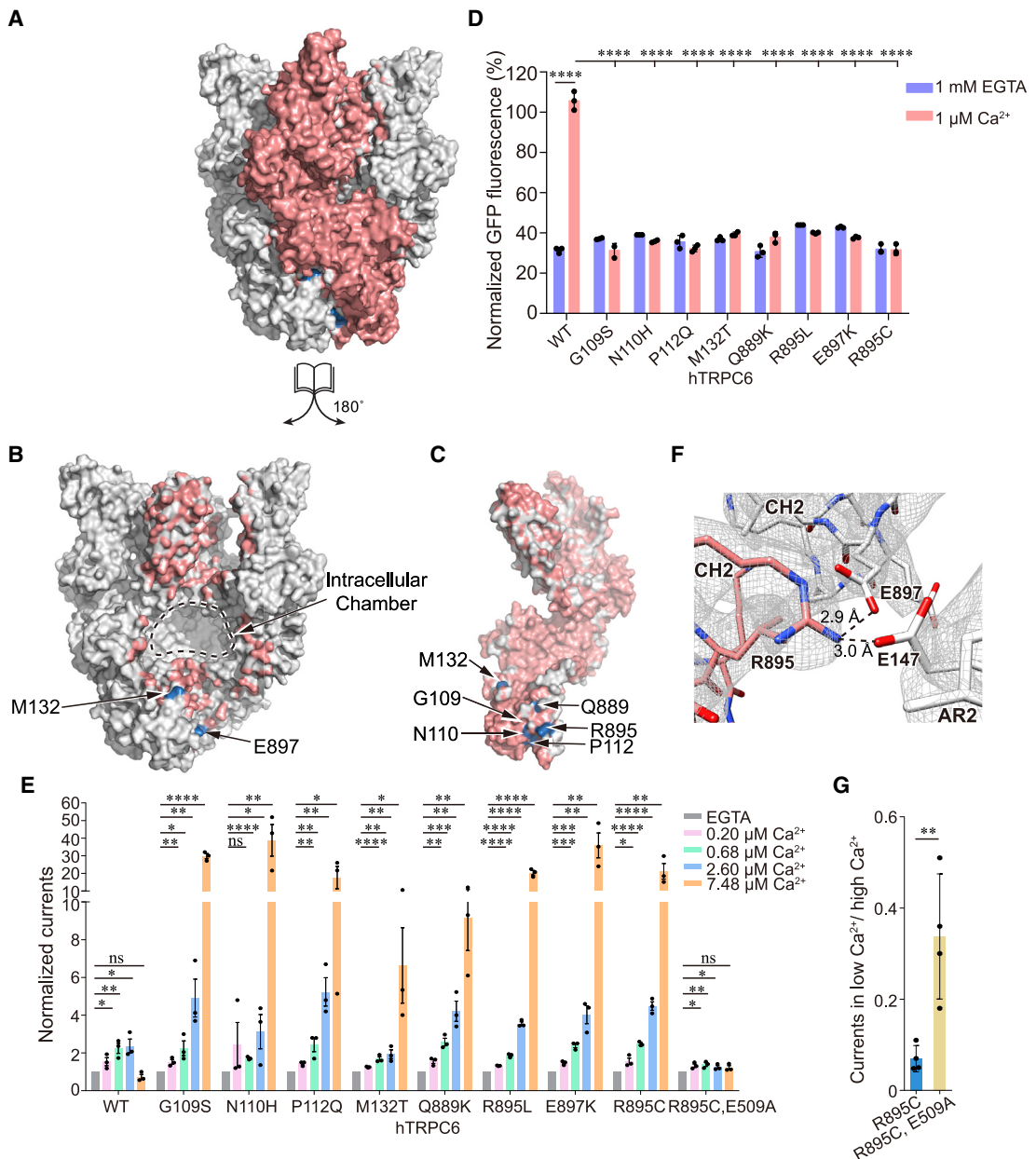
(K) The ratio of OAG-evoked whole-cell currents in low-calcium over high-calcium solution for WT hTRPC6 and CBS1 mutation D890A at holding potential of -60 mV. Two-tailed Student's t test, * $p < 0.05$.

See also Figures S6 and S7 and Table S1.

8H), suggesting that this mutant has impaired calcium inhibition, whereas calcium activation via CBS3 remains intact. Supporting this hypothesis, the additional mutation E509A in CBS3 abolished calcium activation of the R895C mutant (Figures 5E and S8I). Moreover, we found that the extracellular calcium robustly enhanced the OAG-activated whole-cell currents of hTRPC6 R895C mutant at holding potential of -60 mV, whereas additional E509A mutation impaired such enhancement effect of extracellular calcium (Figures 5G, S8M, and S8N), indicating the

enhancement of OAG-activated hTRPC6 currents by extracellular calcium is mediated by CBS3.

To understand the pathogenic mechanism of FSGS mutations at the atomic level, we sought to study the structure of the hTRPC6 R895C mutant. However, due to the structural instability issue of the hTRPC6 TMD, we grafted this mutation into hTRPC3 to generate the R803C mutant of hTRPC3 (as R895C in hTRPC6) for structural studies. Electrophysiological recording and thermostability assays showed that R803C of the hTRPC3 mutant

**Figure 5. hTRPC6 GOF FSGS mutations**

(A–C) The open-book view of the inter-subunit interface of hTRPC6 in surface representation. Subunit A of hTRPC6 is shown in pink, and the remaining three subunits B–D are in gray. Residues interacting with subunit A are colored in pink in (B). Residues interacting with subunits B–D are colored in gray in (C). The positions of GOF FSGS mutations are colored in blue.

(D) Effect of calcium on the thermostability of various hTRPC6 GOF mutants. $n = 3$ biological replicates. The data are shown as the mean \pm SD. Two-tailed Student's t test, * $p < 0.05$, ** $p < 0.01$, *** $p < 0.001$, **** $p < 0.0001$.

(E) Effect of calcium on the currents of various hTRPC6 constructs in inside-out mode. $n = 3$ independent patches and the data are shown as the mean \pm SEM. The data of WT hTRPC6 are the same as in Figure 4I. One-tailed Student's t test, * $p < 0.05$, ** $p < 0.01$, *** $p < 0.001$, **** $p < 0.0001$.

(F) Interactions between R895 and E147 and E897 in hTRPC6.

(G) The ratio of OAG-evoked whole-cell currents in low-calcium over high-calcium solution for hTRPC6 R895C and R895C, E509A mutants, at holding potential of -60 mV. Two-tailed Student's t test, ** $p < 0.01$.

See also Figure S8.

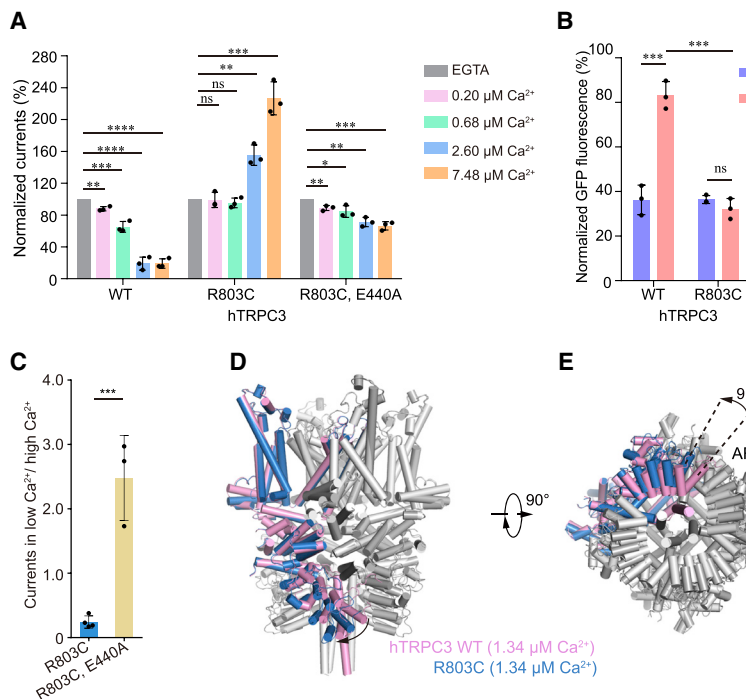


Figure 6. Structures of WT and R803C mutant of hTRPC3 in the presence of 1.34 μM free calcium

(A) The effects of calcium on the currents of various hTRPC3 constructs in inside-out mode. n = 3 independent patches and the data are shown as the mean ± SD. Two-tailed Student's t test, *p < 0.05, **p < 0.01, ***p < 0.001, ****p < 0.0001.

(B) Effect of calcium on the thermostability of hTRPC3 and R803C mutant. n = 3 biological replicates. The data are shown as the mean ± SD. Two-tailed Student's t test, ***p < 0.001.

(C) The ratio of OAG-evoked whole-cell currents in low-calcium over high-calcium solution for hTRPC3 R803C and R803C, E440A mutants, at holding potential of -60 mV. Two-tailed Student's t test, ***p < 0.001.

(D) Structural comparison of WT hTRPC3 and R803C mutant with 1.34 μM calcium shown in side view. TMD is used for structural alignment. Subunit A is colored in pink for WT hTRPC3 and blue for the R803C mutant. The other subunits are in gray. The rotation of ICD is denoted by arrows.

(E) Bottom view of the aligned structures and the rotational angle between AR1 in the two structures is measured.

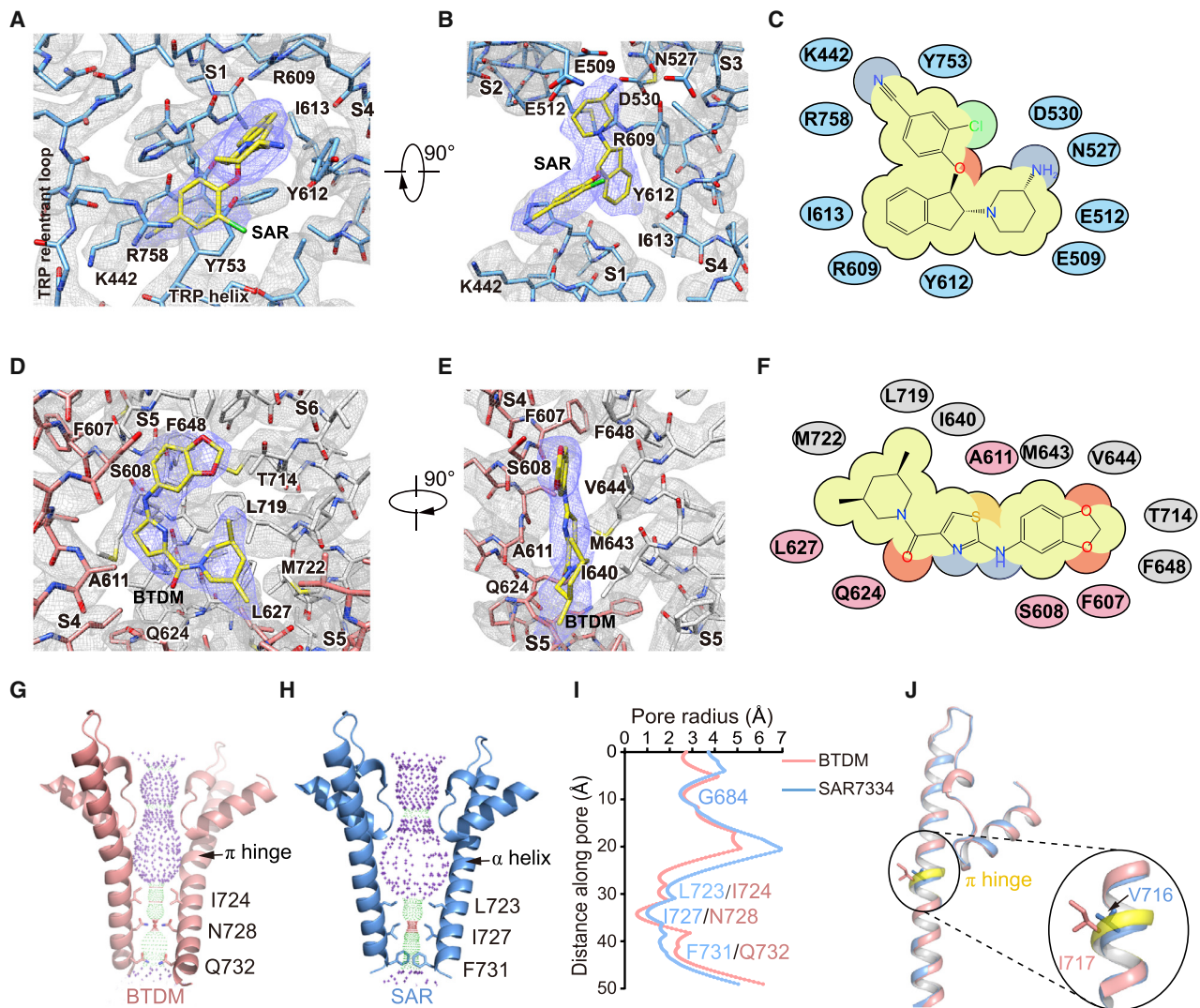
See also Figures S8, S9, S10, and S11 and Table S1.

faithfully recapitulated the phenotype of R895C of hTRPC6 (Figures 6A, 6B, S8J, and S8K), suggesting that hTRPC3 R803C is a qualified surrogate for studying the structural mechanism of hTRPC6 R895C. We found that the E440A mutation of CBS3 on hTRPC3 abolished the activation of the R803C mutant by calcium, confirming that CBS3 is also an activating CBS on hTRPC3 (Figures 6A and S8L). Moreover, we found that the extracellular calcium robustly enhances the whole-cell OAG-activated currents of hTRPC3 R803C at -60 mV, whereas additional E440A mutation impairs the enhancement (Figures 6C, S8O, and S8P), indicating such enhancement is mediated by CBS3. We used 1.34 μM calcium to study the structure of both WT hTRPC3 and R803C mutant because this calcium concentration represents a high-calcium state in the cytosol and can effectively inhibit the basal activity of WT hTRPC3 but not the R803C mutant. We resolved the structures of WT hTRPC3 and the R803C mutant to the resolutions of 3.9 and 3.2 Å, respectively (Figures 6D, 6E, S9, and S10; Table S1). R803C mutant in the presence of 1.34 μM calcium is predominantly in the loosely packed conformation that resembles hTRPC3_{low-calcium} in which both Tunnels A and B are open, allowing hydrated calcium ions to pass through (Figures S11A–S11C). Moreover, CBS1 and CBS2 are disrupted and no strong density for calcium at CBS3 is observed (Figures S11D–S11F). In contrast, with 1.34 μM calcium, WT hTRPC3 shows a tightly packed conformation similar to hTRPC3_{high-calcium} in which Tunnel B in ICD remains closed (Figures S11B and S11C). We found the CBS1 of WT hTRPC3 at 1.34 μM calcium is intact and calcium ion is bound inside CBS1, whereas no strong calcium density at CBS2 or CBS3 is detected, probably due to their low affinity (Figures S11G–S11I). In the TMD, both structures share a similar structure of ion channel pore in the closed state (Figures S11J–S11L).

By comparing these two structures, we found the ARD rotates for 9.8 degrees (Figures 6D and 6E), akin to the conformational changes observed upon calcium binding. These striking structural differences within ICD illustrate that the R895C mutation activates hTRPC6 channels by promoting the loosely packed structure even in the presence of calcium, presumably by disrupting the ARD-CH2 interface and the inhibitory function of CBS1. Because other GOF hTRPC6 mutations found in FSGS located in ICD share the same phenotypes as R895C in terms of calcium activation and reduced thermostability in the presence of calcium (Figure 5), we propose that these mutations activate hTRPC6 via a similar structural mechanism.

Different inhibitors stabilize distinct closed states of hTRPC6 TMD

SAR7334 is an aminoindanol derivative that also inhibits hTRPC6 currents with an IC₅₀ of 9.5 nM (Qu et al., 2017) (Maier et al., 2015). To understand the detailed interactions between SAR7334 and hTRPC6, we resolved the structure of hTRPC6 in complex with SAR7334 to a resolution of 2.9 Å (Figures 7, S12, and S13). The cryo-EM map unambiguously showed that SAR7334 binds within the VSLD (Figures 7A–7C, S12A, and S12B), which is similar to AM-1473 (Figures S12E–S12H) (Bai et al., 2020) but different from BTDM. Surprisingly, the aminopiperidine moiety of SAR7334 completely occupies the activating CBS3 within VSLD and physically blocks calcium binding (Figures S12A and S12B). The 2.9-Å structure of hTRPC6 in complex with BTDM provides the molecular details for BTDM binding (Figures 7D–7F, S12C, and S12D). We compared these two structures and found that although the S6 gates of hTRPC6 in both BTDM and SAR7334 complex structures are closed, the

**Figure 7. The binding sites SAR7334 and BTDM on hTRPC6**

(A and B) Close-up view of the SAR7334 binding site. Subunit A is in blue. SAR7334 is shown as yellow sticks. Densities of SAR7334 and its interacting residues are contoured at 4 σ and presented as purple and gray mesh, respectively.

(C) Interactions between SAR7334 and hTRPC6. Residues that interact with SAR7334 are shown as ovals and colored the same as in (A).

(D and E) Close-up view of the BTDM binding site. Subunits A and D are colored in pink and gray, respectively. BTDM is shown as yellow sticks. Densities of BTDM and its interacting residues are contoured at 4 σ and presented as purple and gray mesh, respectively.

(F) Interactions between BTDM and hTRPC6. Residues that interact with BTDM are shown as ovals and colored the same as in (D).

(G) Side view of the S5-S6 pore region of hTRPC6 in the BTDM-bound structure. The ion permeation pathway along the pore is shown as dots. Only two subunits are shown for clarity.

(H) Side view of the S5-S6 pore region of hTRPC6 in SAR7334-bound structure.

(I) Pore profiles of inhibitor-bound hTRPC6 structures calculated by HOLE.

(J) hTRPC6 in BTDM-bound structure (pink) and SAR7334-bound structure (blue) are aligned. The π hinge is highlighted in yellow. Residues at the hinge are shown as sticks.

See also Figures S12, S13, and S14 and Table S1.

residues aligning the gate are different. In the BTDM-bound structure, the pore is constricted by I724, N728, and Q732 (Figures 7G–7I), whereas, in the SAR7334-bound structure, the pore is constricted by L723, I727, and F731 (Figures 7H and 7I). These differences are due to the structural deviation of

the middle of the S6 helix. S6 is a continuous α helix in the SAR7334-bound structure, whereas the BTDM-bound structure shows a π hinge around I717 (Figure 7J), probably due to the interactions between BTDM and T714, L719, and M722 on S6 (Figures 7D–7F).

DISCUSSION

Calcium is a second messenger that can modulate TRPC channels (Boulay, 2002; Boulay et al., 1999; Friedlova et al., 2010; Kamouchi et al., 1999; Kwon et al., 2007; Lintschinger et al., 2000; Polat et al., 2019; Shi et al., 2004; Zhang et al., 2001; Zitt et al., 1997). Here, by structural biology approaches, we uncovered three intracellular calcium-binding sites, namely CBS1–3, in hTRPC3 and hTRPC6 channels, suggesting that calcium can modulate the basal activity of these channels through direct binding. Both CBS1 and CBS2 are located in the ICD. CBS1 is situated on the interface between ARD and CH2. CBS2 is formed by residues on CH2 and the loop between CH1 and CH2. Calcium binding at CBS1 stabilizes the ICD in a compact tightly packed conformation so that ion permeation through ICD is constricted. This is in agreement with single-channel recordings showing that calcium reduced unitary currents of TRPC6 and TRPC7 (Shi et al., 2004). We estimated calcium potencies on CBS1 using CBS3 mutants (E440A of hTRPC3 and E509A of hTRPC6) of which the activating calcium regulation is abolished. The IC₅₀ of CBS1 is around 0.71 μM for hTRPC3 (Figure S5L) and 4.14 μM for hTRPC6 (Figure S6M). When the intracellular calcium concentration is low, dissociation of calcium ions from CBS1 leads to the electrostatic repulsion and separation of ARD and CH2, resulting in an overall loosely packed structure in which the ion permeation pathways in ICD are widely open (Figures S14A and S14B). Because TRPC channels are permeable to calcium, inhibitory CBS1 provides a built-in negative feedback mechanism for calcium concentration regulation. CBS3 is located within the VSLD and is an activating site for calcium (Figures 4I and 6A) with a more pronounced efficacy in hTRPC6 than hTRPC3 (Figures 5E and 6A). Therefore, CBS3 provides a positive feedback mechanism for calcium regulation (Figure S14C). The basal currents of hTRPC3 or hTRPC6 in response to intracellular calcium concentrations depend on the interplay between the inhibitory CBS1 and activating CBS3, which differ in terms of both potency and efficacy, leading to differential dose-response: monophasic inhibition for hTRPC3 and bell-shape regulation for hTRPC6 (Figures 1C and 4I). The calcium sensors CBS1 and CBS3 are structurally and functionally conserved in hTRPC3 and hTRPC6, probably also in hTRPC7 and even likely in hTRPC4 and hTRPC5, because of their conserved calcium-binding residues. Notably, due to the low open probability of the hTRPC3 channel in the basal state, all of these structures show a closed ion channel pore, but we think that the same structural mechanism for calcium regulation would fully operate during receptor activation of hTRPC3/6 channels, evidenced by the whole-cell recordings of OAG-activated currents (Figures 2G, 4K, 5G, and 6C).

Moreover, our structural and functional studies reveal that GOF FSGS mutations of hTRPC6, as exemplified by R895C, destabilize the ARD-CH2 interface and thus weaken calcium binding at the inhibitory CBS1. Because activating CBS3 is still intact in these mutants, calcium binding at CBS3 results in the positive feedback amplification of calcium signals and finally leads to calcium overload in podocytes and FSGS disease. Furthermore, the mechanism of these GOF mutations suggests that the co-assembly of these mutant channel subunits with

WT channel subunits will generate heteromeric channels with defective ARD-CH2 interfaces and thus impaired calcium inhibition (Figures S14D and S14F), explaining the autosomal dominant behavior of these mutations in heterozygous patients. It is reported that certain loss-of-function mutations, exemplified by G757D, which is close to TMD and away from CBS1, are associated with FSGS (Riehle et al., 2016), but their pathological mechanisms await further investigation.

In contrast to the FSGS mutants that show a loosely packed structure, the CBS1 mutation D890A would relieve the repulsive electrostatic force between D890 on CH2 and E144 on ARD (Figure 4F); therefore, the D890A mutant probably constantly maintains a stable tightly packed structure irrespective of changes in intracellular calcium concentration. This agrees well with the fact that CBS1 mutants D890A (CBS1) of hTRPC6 and the D798A (CBS1) of hTRPC3 have enhanced thermostability (Figures 2F and 4J).

In addition, TRPC channels are activated by both PIP₂ on the plasma membrane and its degradation product DAG (Lemonnier et al., 2008), which is produced by calcium-activated PLCs (Kadamur and Ross, 2013). Therefore, the calcium influx through the hTRPC3/6 channel might activate PLCs to regulate the activity of the hTRPC3/6 channel. Notably, we observed the current kinetics of the same hTRPC6 FSGS mutants in response to high calcium (7.48 μM) are different between patches (Figures S8A and S8G), and the fast inactivation upon high-calcium treatment is irreversible, suggesting the participation of certain metabotropic process, perhaps the activation of PLC by calcium, subsequent hydrolysis of PIP₂, and thus inactivation of TRPC channel.

Finally, we found that high-affinity inhibitors BTDM and SAR7334 bind to distinct pockets within the TMD of hTRPC6 (Figures S14G and S14H) and the binding of SAR7334 precludes calcium binding onto the activating CBS3. However, the conformations of the gating helices S6 are different and involve the α-π transition. Similar α-π transitions of the S6 helix were previously observed in other channels, including TRP channels (Zubcevic and Lee, 2019) at distinct gating states. Therefore, we speculate that BTDM and SAR7334 stabilize hTRPC6 at different non-conductive states to inhibit the channel. These structural observations pave the way for further structure-based drug design to target hTRPC6 GOF mutants found in FSGS.

STAR★METHODS

Detailed methods are provided in the online version of this paper and include the following:

- [KEY RESOURCES TABLE](#)
- [RESOURCE AVAILABILITY](#)
 - Lead contact
 - Materials availability
 - Data and code availability
- [EXPERIMENTAL MODEL AND SUBJECT DETAILS](#)
 - Cell lines
- [METHOD DETAILS](#)
 - Constructs

- Calcium concentration estimation
- Electrophysiology
- Thermostability assay
- Protein expression and purification
- Cryo-EM sample preparation
- Cryo-EM data collection
- Cryo-EM image processing
- Model building
- Quantification and statistical analysis

SUPPLEMENTAL INFORMATION

Supplemental information can be found online at <https://doi.org/10.1016/j.neuron.2021.12.023>.

ACKNOWLEDGMENTS

We thank Dr. Xiaolin Zhang at Dizal Pharmaceutical Company for providing the BTDM inhibitor. We thank Dr. Yiman Li from the lab of Prof. Zhuan Zhou, Prof. Shiqiang Wang, Prof. Youjun Wang, and Dr. Yaxiong Yang for their helpful advice on patch clamp experiments and free calcium concentration measurement. We thank all of the Chen Lab members for their kind help. Cryo-EM data collection was supported by the Electron Microscopy laboratory and the Cryo-EM platform of Peking University with the assistance of Xuemei Li, Zhenxi Guo, Xia Pei, Bo Shao, and Guopeng Wang. Part of the structural computation was also performed on the Computing Platform of the Center for Life Science and High-performance Computing Platform of Peking University. We thank the National Center for Protein Sciences at Peking University in Beijing, China for assistance with negative-stain EM. This work is supported by grants from National Natural Science Foundation of China (91957201, 31870833, and 31821091 to L.C., 31900859 to J.-X.W.), and the China Postdoctoral Science Foundation (2016M600856, 2017T100014, 2019M650324, and 2019T120014 to J.-X.W.). J.-X.W. and Y.K. are supported by the Boya Postdoctoral Fellowship of Peking University. J.-X.W. is also supported by the postdoctoral foundation of the Peking-Tsinghua Center for Life Sciences (CLS), Peking University.

AUTHOR CONTRIBUTIONS

L.C. initiated the project. W.G., Q.T., and M.W. purified protein and prepared the cryo-EM sample. W.G., M.W., Y.K., and J.-X.W. collected the cryo-EM data. W.G. and L.C. processed the data and built and refined the model. W.G. did electrophysiology and thermostability measurements. All authors contributed to the manuscript preparation.

DECLARATION OF INTERESTS

The authors declare no competing interests.

Received: May 4, 2021

Revised: November 9, 2021

Accepted: December 15, 2021

Published: January 19, 2022

REFERENCES

- Abramowitz, J., and Birnbaumer, L. (2009). Physiology and pathophysiology of canonical transient receptor potential channels. *FASEB J* 23, 297–328.
- Adams, P.D., Afonine, P.V., Bunkózzi, G., Chen, V.B., Davis, I.W., Echols, N., Headd, J.J., Hung, L.-W., Kapral, G.J., Grosse-Kunstleve, R.W., et al. (2010). PHENIX: a comprehensive Python-based system for macromolecular structure solution. *Acta Crystallogr. D Biol. Crystallogr.* 66, 213–221.
- Autzen, H.E., Myasnikov, A.G., Campbell, M.G., Asarnow, D., Julius, D., and Cheng, Y. (2018). Structure of the human TRPM4 ion channel in a lipid nanodisc. *Science* 359, 228–232.
- Bai, Y., Yu, X., Chen, H., Horne, D., White, R., Wu, X., Lee, P., Gu, Y., Ghimire-Rijal, S., Lin, D.C.-H., and Huang, X. (2020). Structural basis for pharmacological modulation of the TRPC6 channel. *Elife* 9, e53311.
- Barger, J.P., and Dillon, P.F. (2016). Near-membrane electric field calcium ion dehydration. *Cell Calcium* 60, 415–422.
- Boulay, G. (2002). Ca(2+)-calmodulin regulates receptor-operated Ca(2+) entry activity of TRPC6 in HEK-293 cells. *Cell Calcium* 32, 201–207.
- Boulay, G., Brown, D.M., Qin, N., Jiang, M., Dietrich, A., Zhu, M.X., Chen, Z., Birnbaumer, M., Mikoshiba, K., and Birnbaumer, L. (1999). Modulation of Ca(2+) entry by polypeptides of the inositol 1,4-, 5-trisphosphate receptor (IP3R) that bind transient receptor potential (TRP): evidence for roles of TRP and IP3R in store depletion-activated Ca(2+) entry. *Proc. Natl. Acad. Sci. USA* 96, 14955–14960.
- Chen, X., Sooch, G., Demaree, I.S., White, F.A., and Obukhov, A.G. (2020). Transient receptor potential canonical (TRPC) channels: then and now. *Cells* 9, 1983.
- Chovancova, E., Pavelka, A., Benes, P., Strnad, O., Brezovsky, J., Kozlikova, B., Gora, A., Sustr, V., Klvana, M., Medek, P., et al. (2012). CAVER 3.0: a tool for the analysis of transport pathways in dynamic protein structures. *PLoS Comput. Biol.* 8, e1002708.
- Duan, J., Li, J., Chen, G.-L., Ge, Y., Liu, J., Xie, K., Peng, X., Zhou, W., Zhong, J., Zhang, Y., et al. (2019). Cryo-EM structure of TRPC5 at 2.8-A resolution reveals unique and conserved structural elements essential for channel function. *Sci. Adv.* 5, eaaw7935.
- Duan, J., Li, J., Zeng, B., Chen, G.-L., Peng, X., Zhang, Y., Wang, J., Clapham, D.E., Li, Z., and Zhang, J. (2018). Structure of the mouse TRPC4 ion channel. *Nat. Commun.* 9, 3102.
- Emsley, P., Lohkamp, B., Scott, W.G., and Cowtan, K. (2010). Features and development of coot. *Acta Crystallogr. D Biol. Crystallogr.* 66, 486–501.
- Fan, C., Choi, W., Sun, W., Du, J., and Lü, W. (2018). Structure of the human lipid-gated cation channel TRPC3. *Elife* 7, e36852.
- Feng, S. (2017). TRPC channel structure and properties. *Adv. Exp. Med. Biol.* 976, 9–23.
- Friedlova, E., Grycova, L., Holakova, B., Silhan, J., Janouskova, H., Sulc, M., Obsilova, V., Obsil, T., and Teisinger, J. (2010). The interactions of the C-terminal region of the TRPC6 channel with calmodulin. *Neurochem. Int.* 56, 363–366.
- Gigante, M., Caridi, G., Montemurno, E., Soccio, M., d'Apolito, M., Cerullo, G., Aucella, F., Schirinzi, A., Emma, F., Massella, L., et al. (2011). TRPC6 mutations in children with steroid-resistant nephrotic syndrome and atypical phenotype. *Clin. J. Am. Soc. Nephrol.* 6, 1626–1634.
- Guo, W., and Chen, L. (2019). Recent progress in structural studies on canonical TRP ion channels. *Cell Calcium* 83, 102075.
- Hartmann, J., Dragicevic, E., Adelsberger, H., Henning, H.A., Sumser, M., Abramowitz, J., Blum, R., Dietrich, A., Freichel, M., Flockerzi, V., et al. (2008). TRPC3 channels are required for synaptic transmission and motor coordination. *Neuron* 59, 392–398.
- Hartmann, J., and Konnerth, A. (2015). TRPC3-dependent synaptic transmission in central mammalian neurons. *J. Mol. Med. (Berl.)* 93, 983–989.
- Hattori, M., Hibbs, R.E., and Gouaux, E. (2012). A fluorescence-detection size-exclusion chromatography-based thermostability assay for membrane protein precrystallization screening. *Structure* 20, 1293–1299.
- Huang, Y., Winkler, P.A., Sun, W., Lü, W., and Du, J. (2018). Architecture of the TRPM2 channel and its activation mechanism by ADP-ribose and calcium. *Nature* 562, 145–149.
- Jia, Y., Zhou, J., Tai, Y., and Wang, Y. (2007). TRPC channels promote cerebellar granule neuron survival. *Nat. Neurosci.* 10, 559–567.
- Kadamur, G., and Ross, E.M. (2013). Mammalian phospholipase C. *Annu. Rev. Physiol.* 75, 127–154.
- Kamouchi, M., Philipp, S., Flockerzi, V., Wissenbach, U., Mamin, A., Raeymaekers, L., Eggermont, J., Droogmans, G., and Nilius, B. (1999).

- Properties of heterologously expressed hTRP3 channels in bovine pulmonary artery endothelial cells. *J. Physiol.* 518, 345–358.
- Kwon, Y., Hofmann, T., and Montell, C. (2007). Integration of phosphoinositide- and calmodulin-mediated regulation of TRPC6. *Mol. Cell* 25, 491–503.
- Lemonnier, L., Trebak, M., and Putney, J.W., Jr. (2008). Complex regulation of the TRPC3, 6 and 7 channel subfamily by diacylglycerol and phosphatidylinositol-4,5-bisphosphate. *Cell Calcium* 43, 506–514.
- Li, H.S., Xu, X.Z., and Montell, C. (1999). Activation of a TRPC3-dependent cation current through the neurotrophin BDNF. *Neuron* 24, 261–273.
- Lintscherger, B., Balzer-Geldsetzer, M., Baskaran, T., Graier, W.F., Romanin, C., Zhu, M.X., and Gschner, K. (2000). Coassembly of Trp1 and Trp3 proteins generates diacylglycerol- and Ca²⁺-sensitive cation channels. *J. Biol. Chem.* 275, 27799–27805.
- Maier, T., Follmann, M., Hessler, G., Kleemann, H.-W., Hachtel, S., Fuchs, B., Weissmann, N., Linz, W., Schmidt, T., Löhn, M., et al. (2015). Discovery and pharmacological characterization of a novel potent inhibitor of diacylglycerol-sensitive TRPC cation channels. *Br. J. Pharmacol.* 172, 3650–3660.
- Nikolaev, Y.A., Cox, C.D., Ridone, P., Rohde, P.R., Cordero-Morales, J.F., Vásquez, V., Laver, D.R., and Martinac, B. (2019). Mammalian TRP ion channels are insensitive to membrane stretch. *J. Cell Sci.* 132, jcs238360.
- Pettersen, E.F., Goddard, T.D., Huang, C.C., Couch, G.S., Greenblatt, D.M., Meng, E.C., and Ferrin, T.E. (2004). UCSF Chimera—A visualization system for exploratory research and analysis. *J. Comput. Chem.* 25, 1605–1612.
- Phulera, S., Zhu, H., Yu, J., Claxton, D.P., Yoder, N., Yoshioka, C., and Gouaux, E. (2018). Cryo-EM structure of the benzodiazepine-sensitive $\alpha 1\beta 1\gamma 2S$ tri-heteromeric GABAA receptor in complex with GABA. *Elife* 7, e39383.
- Polat, O.K., Uno, M., Maruyama, T., Tran, H.N., Imamura, K., Wong, C.F., Sakaguchi, R., Ariyoshi, M., Itsuki, K., Ichikawa, J., et al. (2019). Contribution of coiled-coil assembly to Ca²⁺/calmodulin-dependent inactivation of TRPC6 channel and its impacts on FSGS-associated phenotypes. *J. Am. Soc. Nephrol.* 30, 1587–1603.
- Pollak, M.R. (2014). Familial FSGS. *Adv. Chronic Kidney Dis.* 21, 422–425.
- Punjani, A., Rubinstein, J.L., Fleet, D.J., and Brubaker, M.A. (2017). cryoSPARC: algorithms for rapid unsupervised cryo-EM structure determination. *Nat. Methods* 14, 290–296.
- Qu, C., Ding, M., Zhu, Y., Lu, Y., Du, J., Miller, M., Tian, J., Zhu, J., Xu, J., Wen, M., et al. (2017). Pyrazolopyrimidines as potent stimulators for transient receptor potential canonical 3/6/7 channels. *J. Med. Chem.* 60, 4680–4692.
- Reiser, J., Polu, K.R., Möller, C.C., Kenlan, P., Altintas, M.M., Wei, C., Faul, C., Herbert, S., Villegas, I., Avila-Casado, C., et al. (2005). TRPC6 is a glomerular slit diaphragm-associated channel required for normal renal function. *Nat. Genet.* 37, 739–744.
- Riehle, M., Büscher, A.K., Gohlke, B.-O., Kaßmann, M., Kolatsi-Joannou, M., Bräsen, J.H., Nagel, M., Becker, J.U., Winyard, P., Hoyer, P.F., et al. (2016). TRPC6 G757D loss-of-function mutation associates with FSGS. *J. Am. Soc. Nephrol.* 27, 2771–2783.
- Shi, J., Mori, E., Mori, Y., Mori, M., Li, J., Ito, Y., and Inoue, R. (2004). Multiple regulation by calcium of murine homologues of transient receptor potential proteins TRPC6 and TRPC7 expressed in HEK293 cells. *J. Physiol.* 561, 415–432.
- Smart, O.S., Goodfellow, J.M., and Wallace, B.A. (1993). The pore dimensions of gramicidin A. *Biophys. J.* 65, 2455–2460.
- Smart, O.S., Neduvelli, J.G., Wang, X., Wallace, B.A., and Sansom, M.S.P. (1996). HOLE: A program for the analysis of the pore dimensions of ion channel structural models. *Journal of Molecular Graphics* 14, 354–360.
- Song, K., Wei, M., Guo, W., Quan, L., Kang, Y., Wu, J.-X., and Chen, L. (2021). Structural basis for human TRPC5 channel inhibition by two distinct inhibitors. *Elife* 10, e63429.
- Tang, Q., Guo, W., Zheng, L., Wu, J.-X., Liu, M., Zhou, X., Zhang, X., and Chen, L. (2018). Structure of the receptor-activated human TRPC6 and TRPC3 ion channels. *Cell Res.* 28, 746–755.
- Vinayagam, D., Quentin, D., Yu-Strzelczyk, J., Sitsel, O., Merino, F., Stabrin, M., Hofnagel, O., Yu, M., Leedeboer, M.W., Nagel, G., et al. (2020). Structural basis of TRPC4 regulation by calmodulin and pharmacological agents. *Elife* 9, e60603.
- Wang, L., Fu, T.-M., Zhou, Y., Xia, S., Greka, A., and Wu, H. (2018). Structures and gating mechanism of human TRPM2. *Science* 362, eaav4809.
- Wes, P.D., Chevesich, J., Jeromin, A., Rosenberg, C., Stetten, G., and Montell, C. (1995). TRPC1, a human homolog of a Drosophila store-operated channel. *Proc. Natl. Acad. Sci. USA* 92, 9652–9656.
- Winn, M.P., Conlon, P.J., Lynn, K.L., Farrington, M.K., Creazzo, T., Hawkins, A.F., Daskalakis, N., Kwan, S.Y., Ebersviller, S., Burchette, J.L., et al. (2005). A mutation in the TRPC6 cation channel causes familial focal segmental glomerulosclerosis. *Science* 308, 1801–1804.
- Zhang, K. (2016). Gctf: real-time CTF determination and correction. *J. Struct. Biol.* 193, 1–12.
- Zhang, Z., Tang, J., Tikunova, S., Johnson, J.D., Chen, Z., Qin, N., Dietrich, A., Stefani, E., Birnbaumer, L., and Zhu, M.X. (2001). Activation of Trp3 by inositol 1,4,5-trisphosphate receptors through displacement of inhibitory calmodulin from a common binding domain. *Proc. Natl. Acad. Sci. USA* 98, 3168–3173.
- Zhang, Z., Tóth, B., Szollosi, A., Chen, J., and Csanády, L. (2018). Structure of a TRPM2 channel in complex with Ca²⁺ explains unique gating regulation. *Elife* 7, e36409.
- Zheng, S.Q., Palovcak, E., Armache, J.-P., Verba, K.A., Cheng, Y., and Agard, D.A. (2017). MotionCor2: anisotropic correction of beam-induced motion for improved cryo-electron microscopy. *Nat. Methods* 14, 331–332.
- Zhou, J., Du, W., Zhou, K., Tai, Y., Yao, H., Jia, Y., Ding, Y., and Wang, Y. (2008). Critical role of TRPC6 channels in the formation of excitatory synapses. *Nat. Neurosci.* 11, 741–743.
- Zhu, X., Chu, P.B., Peyton, M., and Birnbaumer, L. (1995). Molecular cloning of a widely expressed human homologue for the Drosophila trp gene. *FEBS Lett.* 373, 193–198.
- Zitt, C., Obukhov, A.G., Strübing, C., Zobel, A., Kalkbrenner, F., Lückhoff, A., and Schultz, G. (1997). Expression of TRPC3 in Chinese hamster ovary cells results in calcium-activated cation currents not related to store depletion. *J. Cell Biol.* 138, 1333–1341.
- Zivanov, J., Nakane, T., Forsberg, B.O., Kimanis, D., Hagen, W.J., Lindahl, E., and Scheres, S.H. (2018). New tools for automated high-resolution cryo-EM structure determination in RELION-3. *Elife* 7, e42166.
- Zubcevic, L., and Lee, S.-Y. (2019). The role of pi-helices in TRP channel gating. *Curr. Opin. Struct. Biol.* 58, 314–323.

STAR★METHODS

KEY RESOURCES TABLE

REAGENT or RESOURCE	SOURCE	IDENTIFIER
Chemicals, peptides, and recombinant proteins		
Lauryl Maltose Neopentyl Glycol (LMNG)	Anatrace	NG310
Cholesteryl Hemisuccinate Tris Salt (CHS)	Anatrace	CH210
glyco-diosgenin (GDN)	Anatrace	GDN101
fluorinated octyl-maltoside (FOM)	Anatrace	O310F
sf-900 III SFM medium	Thermo Fisher Scientific	Cat#12658-027
Cellfectin II reagents	Thermo Fisher Scientific	Cat#10362-100
SMM 293-TI	Sino Biological Inc.	M293TI
SIM SF Expression Medium	Sino Biological Inc	MSF1
PEI	Polysciences	23966
BTDM	Dizal pharmaceutical company	N/A
SAR7334	<u>Tocris Bioscience</u>	Cat. No. 5831
Calcium Calibration Buffer Kit	<u>Biotium</u>	#59100
Fura-2 potassium salt	Invitrogen	F1200
Fluo-3 FF, pentapotassium salt	AAT Bioquest	21019
graphene oxide	sigma-aldrich	763705
Critical commercial assays		
amylose resin	NEB	E8022L
Superose 6, 10/300 GL	GE Healthcare	17-5172-01
Deposited data		
Coordinates of hTRPC3 in high calcium state	This paper	7DXB
Coordinates of hTRPC3 in low calcium state	This paper	7DXC
Coordinates of hTRPC3 in 1.34 micromolar calcium state	This paper	7DXD
Coordinates of hTRPC3 R803C mutant in 1.34 micromolar calcium state	This paper	7DXE
Coordinates of BTDM-bound hTRPC6 in high calcium state	This paper	7DXF
Coordinates of SAR7334-bound hTRPC6 in high calcium state	This paper	7DXG
Cryo-EM map of hTRPC3 in high calcium state	This paper	EMD-30903
Cryo-EM map of hTRPC3 in low calcium state	This paper	EMD-30904
Cryo-EM map of hTRPC3 in 1.34 micromolar calcium state	This paper	EMD-30905
Cryo-EM map of hTRPC3 R803C mutant in 1.34 micromolar calcium state	This paper	EMD-30906
Cryo-EM map of BTDM-bound hTRPC6 in high calcium state	This paper	EMD-30907
Cryo-EM map of SAR7334-bound hTRPC6 in high calcium state	This paper	EMD-30908
Experimental models: Cell lines		
Sf9	Thermo Fisher Scientific	12659017
HEK293F	Thermo Fisher Scientific	R79007

(Continued on next page)

Continued

REAGENT or RESOURCE	SOURCE	IDENTIFIER
Recombinant DNA		
hTRPC3 cloned into a modified N-terminal GFP-tagged BacMam vector for electrophysiology and thermostability assay	Tang et al., 2018.	N/A
hTRPC3 cloned into a N-terminal GFP-MBP (Maltose Binding Protein)-tagged BacMam vector for expression in mammalian cells	This paper	N/A
hTRPC3 R803C mutant cloned into a N-terminal GFP-MBP (Maltose Binding Protein)-tagged BacMam vector for expression in mammalian cells	This paper	N/A
hTRPC6 cloned into a N-terminal GFP-MBP (Maltose Binding Protein)-tagged BacMam vector for expression in mammalian cells	This paper	N/A
truncated hTRPC6 (72-904 aa) cloned into a modified N-terminal GFP-tagged BacMam vector for expression in mammalian cells	Tang et al., 2018 PMID: 29700422.	N/A
Software and Algorithms		
Gctf_v1.18	Zhang, 2016	Zhang Software - MRC Laboratory of Molecular Biology (cam.ac.uk)
Gautomatch v0.56	kindly provided by Kai Zhang	Zhang Software - MRC Laboratory of Molecular Biology (cam.ac.uk)
RELION-3.0	Zivanov et al., 2018	Relion (cam.ac.uk)
PHENIX 1.18.1-3865	Adams et al., 2010	https://www.phenix-online.org/
HOLE2 v2.2.005	(Smart et al., 1996)	HOLE program homepage
cryoSPARC v3.1	Punjani et al., 2017	http://cryosparc.com
Pymol	Schrödinger, LLC	http://www.pymol.org
Chimera-1.13	(Pettersen et al., 2004)	http://www.cgl.ucsf.edu/chimera
COOT	Emsley et al., 2010	http://www2.mrc-lmb.cam.ac.uk/Personal/pemsley/coot
Other		
Quantifoil (0.6/1) gold grids, 300Au	Quantifoil	N/A

RESOURCE AVAILABILITY**Lead contact**

Further information and requests for resources and reagents should be directed to and will be fulfilled by Lei Chen (chenlei2016@pku.edu.cn).

Materials availability

All unique reagents generated in this study are available from the lead contact with a completed Materials Transfer Agreement.

Data and code availability

All of the cryo-EM maps and atomic coordinates produced from this study have been deposited into Electron Microscopy Data Bank and Protein Data Bank with accession numbers:hTRPC3 in high-calcium state (EMD-30903, PDB: 7DXB), hTRPC3 in low-calcium state (EMD-30904, PDB: 7DXC), hTRPC3 with 1.34 μM free calcium (EMD-30905, PDB: 7DXD), hTRPC3 R803C mutant with 1.34 μM free calcium (EMD-30906, PDB: 7DXE), BTDM-bound hTRPC6 (EMD-30907, PDB: 7DXF), and SAR7334-bound hTRPC6 (EMD-30908, PDB: 7DXG). They are publicly available as of the date of publication. Accession numbers are also listed in the key resources table.

This paper does not report original code.

Any additional information required to reanalyze the data reported in this work paper is available from the lead contact upon request.

EXPERIMENTAL MODEL AND SUBJECT DETAILS

Cell lines

Sf9 cells were cultured in Sf-900 III SFM medium (Gibco) at 27°C. HEK293F cells grown in FreeStyle 293 medium + 1% FBS, at 37°C were transfected for electrophysiology and thermostability. HEK293F cells grown in SMM-293TI medium + 1% FBS, at 37°C were used for baculovirus infection and protein purification.

METHOD DETAILS

Constructs

The cDNA of hTRPC3 and hTRPC6 were cloned into a modified N-terminal GFP-tagged BacMam vector for electrophysiology and thermostability assay as described previously (Tang et al., 2018). The cDNA of WT full-length hTRPC3, hTRPC3 R803C mutant, and WT full-length hTRPC6 were inserted into an N-terminal GFP-MBP (Maltose Binding Protein)-tagged BacMam vector, and truncated hTRPC6 (72-904 aa) was inserted into N-terminal GFP-tagged BacMam vector for protein purification. Wild type calmodulin and its mutant (D21A+D57A+D94A+D130A, CaM-4DA) were cloned into the BacMam vector for co-expression with the hTRPC3 channel.

Calcium concentration estimation

Standard solutions with free Ca^{2+} concentration ranging from 0 to 39 μM was prepared by mixing solution A (10 mM K_2EGTA , 100 mM KCl, and 30 mM MOPS, pH 7.2) and solution B (10 mM CaEGTA , 100 mM KCl and 30 mM MOPS, pH 7.2) from Biotium company. 1 μM fura-2 was added into standard solution (calcium concentration ranges from 0 to 1.35 μM) and fluorescence at excitation 340 nm and 380 nm and emission at 510 nm were measured using Tecan instrument to generate a calibration curve. 1 μM fluo-3FF was added into standard solution (calcium concentration ranges from 1.35 to 39 μM) and fluorescence at excitation 475 nm and emission at 530 nm using Tecan instrument to generate a calibration curve. Solutions for electrophysiology were supplemented with either 1 μM fura-2 or 1 μM fluo-3FF and their fluorescence was measured and mapped onto the calibration curve accordingly.

Electrophysiology

The effects of cytosolic calcium on TRPC were measured by patch-clamp in inside-out mode. The bath solutions with different calcium concentrations were prepared by titrating buffer A (140 NaCl, 10 HEPES, 1 EGTA in mM, pH=7.4 adjusted by NaOH) into buffer B (140 NaCl, 10 HEPES, 1 EGTA, 1 CaCl_2 in mM, pH=7.4 adjusted by NaOH) and calcium concentrations were estimated using fluorescent calcium dye as described above. Patch electrodes were pulled by a horizontal microelectrode puller (P-1000, Sutter Instrument Co, USA) to a tip resistance of 1.0-3.0 $\text{M}\Omega$. An MPS-2 perfusion system (Yibo Company, Wuhan, China) was used for buffer change. For inside-out recording, the pipette solution was 140 NaCl, 1 EGTA, 10 HEPES (pH=7.4, adjusted by NaOH) in mM. TRPC currents were recorded at a holding potential of +60 mV through an Axopatch 200B amplifier (Axon Instruments, USA). Data were further analyzed by pCLAMP 10.4 software. Normalized currents (%) = $100 \times (I_{\text{Ca}} - I_{\text{BTDM}}) / (I_{\text{bath}} - I_{\text{BTDM}})$, where I_{Ca} is the steady-current measured at the end of a particular concentration of free calcium, I_{bath} is the control current measured just recovered by bath buffer after calcium effect and I_{BTDM} is the current measured at the end of inhibitor BTDM. The calcium potencies of CBS1 were estimated using CBS3 mutants (E440A for hTRPC3 and E509A for hTRPC6). The calcium concentration of the EGTA buffer was calculated using fura-2 as 0.02 μM . The curve was fitted with dose-response curve: $Y = 100 / (1 + 10^{((\log IC_{50}) - X) * \text{HillSlope}})$. The curve fitting was performed using GraphPad Prism software.

For ramp recording in inside-out mode, WT TRPC currents were induced by a 400 ms voltage ramp protocol (from -80 mV to +80 mV) every 5 seconds at a holding potential of +60 mV. Once the basal currents were stabilized, the recording chamber was perfused with external solutions containing different concentrations of free calcium.

For whole-cell recordings, we used 1-Oleoyl-2-acetyl-sn-glycerol (OAG) to activate the TRPC channel. The pipette solution was 110 CsMe ([cesium,methanesulfonate](#)), 25 CsCl, 2 MgCl_2 , 3.62 CaCl_2 , 10 EGTA and 30 HEPES (pH=7.4 adjusted by CsOH) in mM, in which the free calcium was measured as 160 nM. The high calcium bath solution contains 140 NaCl, 5 CsCl, 2 mM CaCl_2 , 1 MgCl_2 , 10 Glucose and 10 HEPES (pH=7.4, adjusted by NaOH) in mM. The low calcium bath solution contains 140 NaCl, 5 CsCl, 10 EGTA, 1 MgCl_2 , 10 Glucose and 10 HEPES (pH=7.4, adjusted by NaOH) in mM. We used 50 μM OAG in low calcium solution (10 mM EGTA, about 5 nM calcium) to activate hTRPC3, 50 μM OAG in high calcium solution (2 mM CaCl_2) to activate hTRPC6 and BTDM to block the hTRPC3/6 specific currents. Patch electrodes were pulled to a tip resistance of 2.0-4.0 $\text{M}\Omega$ for recording. The TRPC currents were recorded at a holding potential of -60 mV. Data were further analyzed similarly, as aforementioned. To measure the inhibition effects of extracellular calcium on the DAG-activated hTRPC3/6 currents, 20 μM OAG in bath solution was used to evoke the whole-cell currents, and cells were consecutively activated by OAG in high calcium solution and OAG in low calcium solution. The TRPC currents were recorded at a holding potential of -60 mV or +60 mV. Peak currents were used for calculation. To measure the activation effects of extracellular calcium on the DAG-activated hTRPC6 currents, 0.5 μM OAG in bath solution was used to evoke the whole-cell currents, and cells were sequentially activated by OAG in high calcium solution (2 mM CaCl_2) and OAG in low calcium solution (10 mM EGTA or 1 mM EGTA). The pipette solution was 110 CsMe ([cesium,methanesulfonate](#)), 25 CsCl, 2 MgCl_2 , 0.009 CaCl_2 , 0.5 EGTA and 30 HEPES (pH=7.4 adjusted by CsOH) in mM, in which the free calcium was measured as 100 nM. The TRPC currents were recorded at a holding potential of -60 mV.

Thermostability assay

Highly purified non-tagged hTRPC3 protein in 10 mM MNG, 0.1%CHS, TBS (20 mM Tris pH 8.0 at 4°C, 150 mM NaCl) buffer was used for thermostability assay. Diluted protein was divided into three aliquots. One aliquot was supplemented with 1mM EGTA and heated at 50°C for 10 min as the low-calcium heated sample. One aliquot was supplemented with 0.6 μ M free calcium and heated at 50°C for 10 min as the high-calcium heated sample. The remaining aliquot was kept on ice as the non-heated control sample. All samples were centrifuged at 25,000 rpm for 30 min, and supernatants were loaded onto Superose 6 increase column (GE Healthcare) for FSEC analysis. The remaining tetrameric TRPC peak height of the heated sample was divided by the peak height of the non-heated sample. The experiments were independently repeated 3 times.

Highly purified non-tagged hTRPC6 protein in 10 mM MNG, 0.1%CHS, TBS (20 mM Tris pH 8.0 at 4°C, 150 mM NaCl) buffer was also used for thermostability assay. Protein in 1 mM EGTA (low-calcium) or 1 μ M free calcium (high-calcium) was heated at 43°C for 10 min before FSEC. The experiments were independently repeated 3 times for each construct.

For cell lysate samples, different constructs of hTRPC3/6 were transfected into HEK293F cells. 40 h post-transfection, cells were solubilized with 10 mM MNG, 0.1% CHS in TBS buffer for 30 min on ice. Cell lysates from transfected cells were centrifuged at 40,000 rpm for 10 min and then divided into 3 aliquots. Supernatants of hTRPC3 CBS mutants were heated at 48°C for 10 min and hTRPC3 GOF mutants were heated at 45°C for 10 min. Supernatants of hTRPC6 CBS mutants were heated at 46°C for 10 min and hTRPC6 GOF mutants were heated at 41°C for 10 min. All samples were further centrifuged at 40,000 rpm for 30 min before the FSEC analysis. The experiments were independently repeated 3 times for each construct.

Protein expression and purification

HEK293F cells grown in SMM-293TI medium at 37°C with a density of 2.6×10^6 ml $^{-1}$ were infected by BacMam viruses. 10 mM sodium butyrate and 100 nM BTDM were added 10 hours post-infection and the temperature was lowered to 30°C. Cells were collected 48 hours post-infection and washed twice with TBS buffer before frozen at -80°C.

For purification of hTRPC3 protein, cell pellets were solubilized in 10 mM MNG, 0.1% CHS, 100 nM BTDM and protease inhibitors in TBS buffer and rotated at 4°C for 1 h. After centrifugation at 40,000 rpm for 40 min in the Type70 rotor (Beckman), the supernatant was loaded onto a column packed with amylose resin (NEB). The resin was washed by 40 μ M GDN, 0.01 mg/ml soybean lipids, 100 nM BTDM, 10 mM MgCl₂, 1 mM ATP, and 4 mM DTT in TBS buffer to remove heat shock proteins. Protein was eluted with 100 mM maltose in TBS buffer supplemented with 40 μ M GDN, 0.01 mg/ml soybean lipids, 100 nM BTDM, 4 mM DTT, and concentrated using 100-kDa cut-off concentrator (Millipore). After incubation with H3CV protease and PNGase F at 4°C overnight, the concentrated protein was loaded onto Superose 6 increase (GE Healthcare) running in TBS buffer supplemented with 40 μ M GDN, 0.01 mg/ml soybean lipids, 100 nM BTDM, and 1 mM TCEP. The peak fractions containing tetrameric hTRPC3 channel protein were combined and concentrated for nanodisc assembly. hTRPC3 protein, MSP2N2, soybean lipids were mixed at a molar ratio of 1:7:225, and nanodisc samples were assembled as described previously (Tang et al., 2018). After assembly, the mixture was loaded onto a Superose-6 increase column running in TBS containing 1 mM TCEP to remove empty nanodisc. The peak fractions that contain the tetrameric hTRPC3 channel in nanodiscs were combined and concentrated for cryo-EM studies. The GOF mutation of hTRPC3 (R803C) was expressed and purified using the same protocol.

For the sample of hTRPC3 in a low-calcium state, the expression and purification process was the same as described above, except 1mM EDTA was added after the amylose resin.

The hTRPC6 in complex with BTDM in nanodiscs were prepared as previously (Tang et al., 2018), except the functional truncated hTRPC6 (72-904 aa) (Tang et al., 2018) was used.

To prepare the hTRPC6 sample in complex with SAR7334, full-length hTRPC6 virus was used for hTRPC6 channel expression. 10 mM sodium butyrate and 1 μ M SAR7334 were added into the cells 12 hours post-infection and the temperature was lowered to 30°C. Cells were collected 48 h post-infection for further purification. After solubilizing in 10 mM MNG, 0.1% CHS, 1 μ M SAR7334, and protease inhibitors in TBS buffer for 1 h at 4°C, the cell debris was removed by centrifugation at 40,000 rpm for 40 min in Type70 rotor. The supernatant was loaded onto the amylose resin as previously mentioned. 1 μ M SAR7334 were included throughout purification. After cleavage by H3CV protease and PNGase F, further purified by Superose 6 increase column, the peak fractions containing tetrameric hTRPC6 channel protein were combined for cryo-EM.

Cryo-EM sample preparation

The purified tetrameric hTRPC3 in nanodiscs, hTRPC6 with BTDM in nanodiscs were concentrated to A280 = 1.7 and hTRPC6 with SAR7334 was concentrated to A280 = 0.9 with additional 1 mM CaCl₂ and 0.5 mM fluorinated octyl-maltoside (FOM). Protein were added onto Quantifoil (0.6/1) gold grids coated with graphene oxide (Phulera et al., 2018).

The purified tetrameric hTRPC3 nanodiscs in 1mM EDTA were concentrated to A280 = 7 and 1 mM EGTA and 0.5 mM FOM were supplemented into the sample. After centrifugation at 25,000 rpm for 30 min, the protein sample was loaded on Quantifoil 0.6/1 gold 300 mesh grids and blotted using FEI vitrobot. The wild type hTRPC3 nanodisc and hTRPC3 R803C mutant nanodisc were also concentrated to A280=7, and the cryo-EM samples were prepared in a similar procedure except that the free calcium concentration was kept at 1.34 μ M.

Cryo-EM data collection

The prepared cryo-EM grids were firstly screened on Talos Arctica electron microscope (Thermo Fisher Scientific) operating at 200 kV using a K2 camera (Thermo Fisher Scientific). The images of the screened grids were collected on Titan Krios (Thermo Fisher) with a K2 Summit direct electron camera (Thermo Fisher Scientific) and an energy filter set to a slit width of 20 eV at a magnification of 130,000 \times with a pixel size of 0.5225 Å and the defocus ranging from -1.5 µm to -2 µm. Super-resolution movies (32 frames per movie) were collected automatically using Serial EM with a dose rate of 6.25 e-/pixel/s on the detector and a total dose of 48 e-/Å².

Cryo-EM image processing

Movies were first gain-corrected, motion-corrected, anisotropic magnification corrected, dose-weighted by MotionCor2 (Zheng et al., 2017). CTF estimation was done using GCTF (Zhang, 2016). The low-pass filtered projections of the published map of hTRPC6 were used as templates for particle picking using Gautomatch. 2D and 3D classification were carried out using Relion 3.0 (Zivanov et al., 2018). Selected particles were imported into cryoSPARC (Punjani et al., 2017) for ab initio 3D reconstruction using 4 classes and C1 symmetry. Particles from major classes were used for homogeneous refinement using C4 symmetry in cryoSPARC. The resolution estimation was based on the gold standard FSC 0.143 cut-off.

Model building

These hTRPC3/6 models were manually rebuilt using Coot (Emsley et al., 2010) based on the published models 6CUD and 5YX9. These structures were further refined using PHENIX (Adams et al., 2010). Permeation pathways were calculated with HOLE (Smart et al., 1993). Tunnels in the CTD were estimated using CAVER (Chovancova et al., 2012).

Quantification and statistical analysis

Data processing and statistical analysis were conducted using the software GraphPad Prism. Statistical details could be found in the methods details and figure legends. The inside-out currents above 100 pA were used for further analysis. For dose-response recordings, data from Hill fits were represented as mean ± SD (n represents the number of patches). The Student's t test was performed to evaluate differences in calcium response of currents or thermostability.

Neuron, Volume 110

Supplemental information

**Structural mechanism of human TRPC3
and TRPC6 channel regulation by their
intracellular calcium-binding sites**

Wenjun Guo, Qinglin Tang, Miao Wei, Yunlu Kang, Jing-Xiang Wu, and Lei Chen

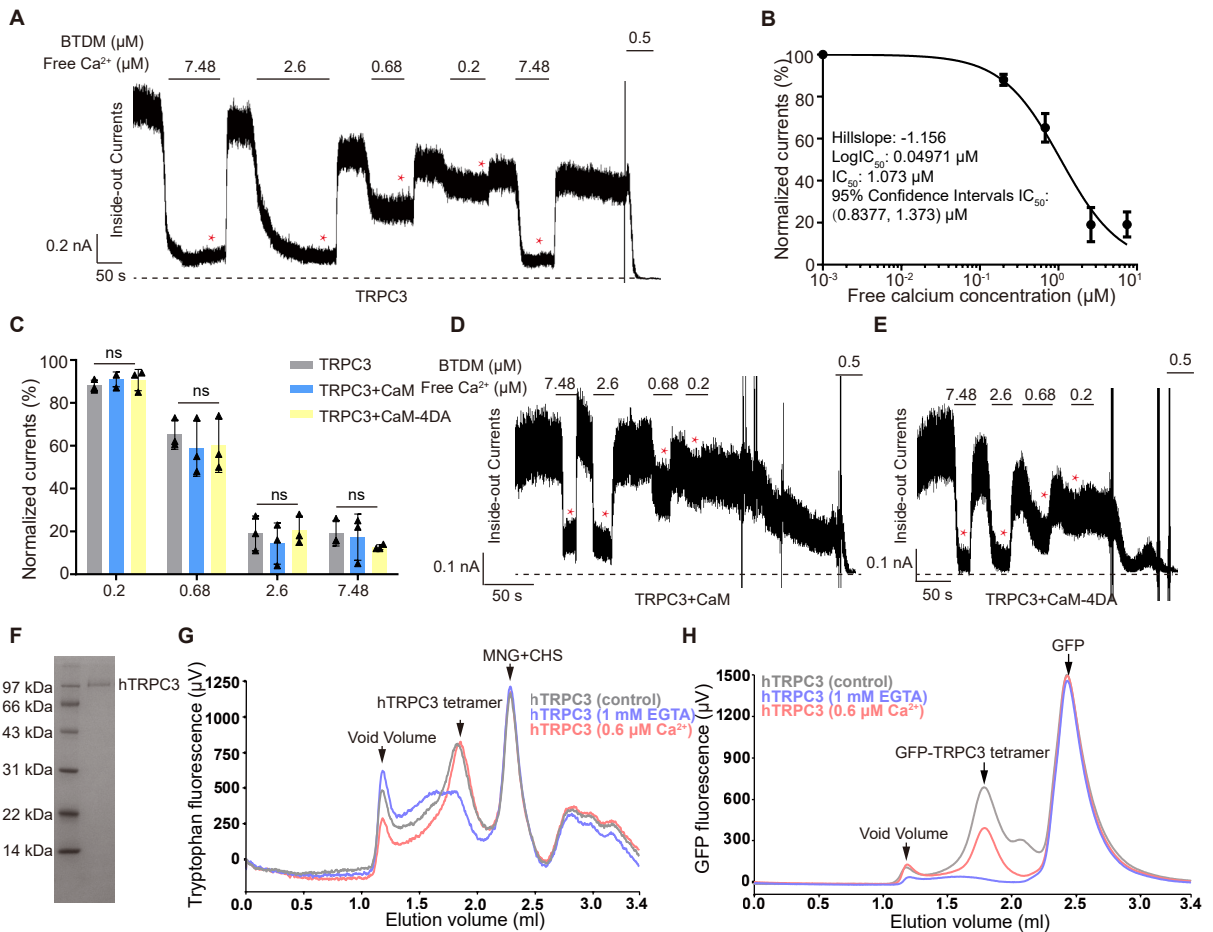


Figure S1 | Calcium regulation of hTRPC3. Related to Figure 1.

(A) Macroscopic currents of wild-type hTRPC3 recorded in the inside-out mode. Zero current is indicated by a dashed line. The currents used for calculations are labeled by asterisks.

(B) Dose-response curve for calcium inhibition of wild type hTRPC3 overexpressed in HEK293F cells. Data are shown as mean \pm SD, n=3 individual patches.

(C) The effects of intracellular calcium on hTRPC3 currents co-transfected with wild-type calmodulin or its mutant (CaM-4DA) measured in the inside-out mode. The data were expressed as the mean \pm SD (n=3 individual patches). Student's t-test, two-tailed.

(D-E) Macroscopic currents of hTRPC3 co-transfected with wild type calmodulin or its mutant (CaM-4DA) recorded in the inside-out mode. Zero current is indicated by a dashed line. The currents used for quantifications are labeled by asterisks.

(F) SDS-PAGE of purified hTRPC3 channel protein used for thermostability measurements.

(G) Representative FSEC profile of purified hTRPC3 after heated at 50°C for 10 min with or without 0.6 μM calcium.

(H) Representative FSEC profile of hTRPC3 cell lysates after heating at 45°C for 10 min with or without 0.6 μM calcium.

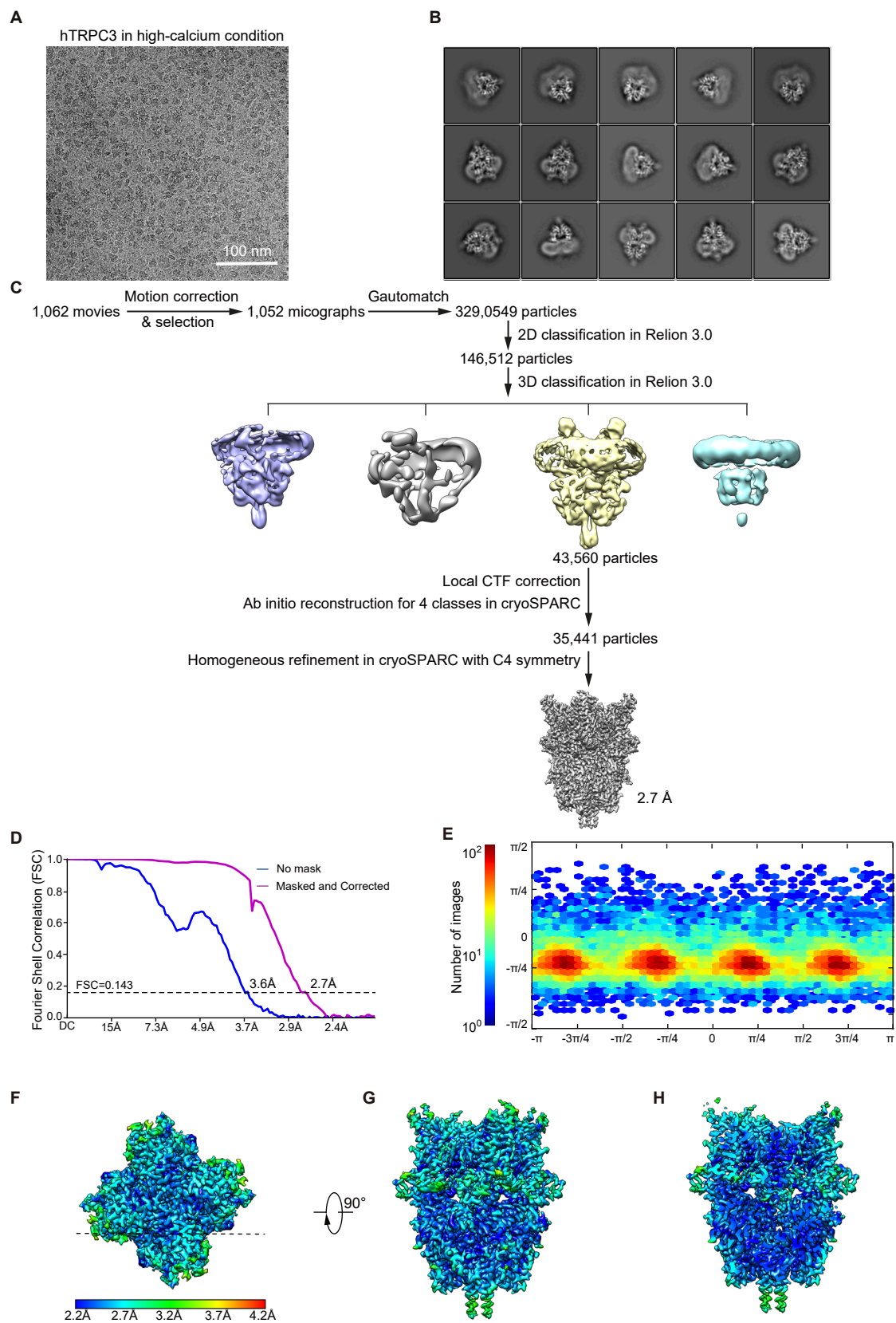


Figure S2 | Cryo-EM image analysis of hTRPC3 in the high-calcium state. Related to Figure 1.

- (A) Representative raw micrograph of hTRPC3 in the high-calcium state.
- (B) Representative 2D class average of hTRPC3 in the high-calcium state.
- (C) Cryo-EM image processing flowchart of hTRPC3 in the high-calcium state.
- (D) Gold-standard FSC curves of final refinement for hTRPC3 in the high-calcium state (C4 symmetry) after correcting for masking effects. Resolution estimations were based on the criterion of the FSC 0.143 cutoff.
- (E) Angular distribution of final refinement for hTRPC3 in the high-calcium state. This is a standard output from cryoSPARC.
- (F) Local resolution estimation of hTRPC3 in the high-calcium state from the top view.
- (G) Side view of local resolution estimation of hTRPC3 in the high-calcium state.
- (H) The cross-section of local resolution estimation of hTRPC3 in the high-calcium state. The position of the cross-section is indicated by a dashed line in (F).

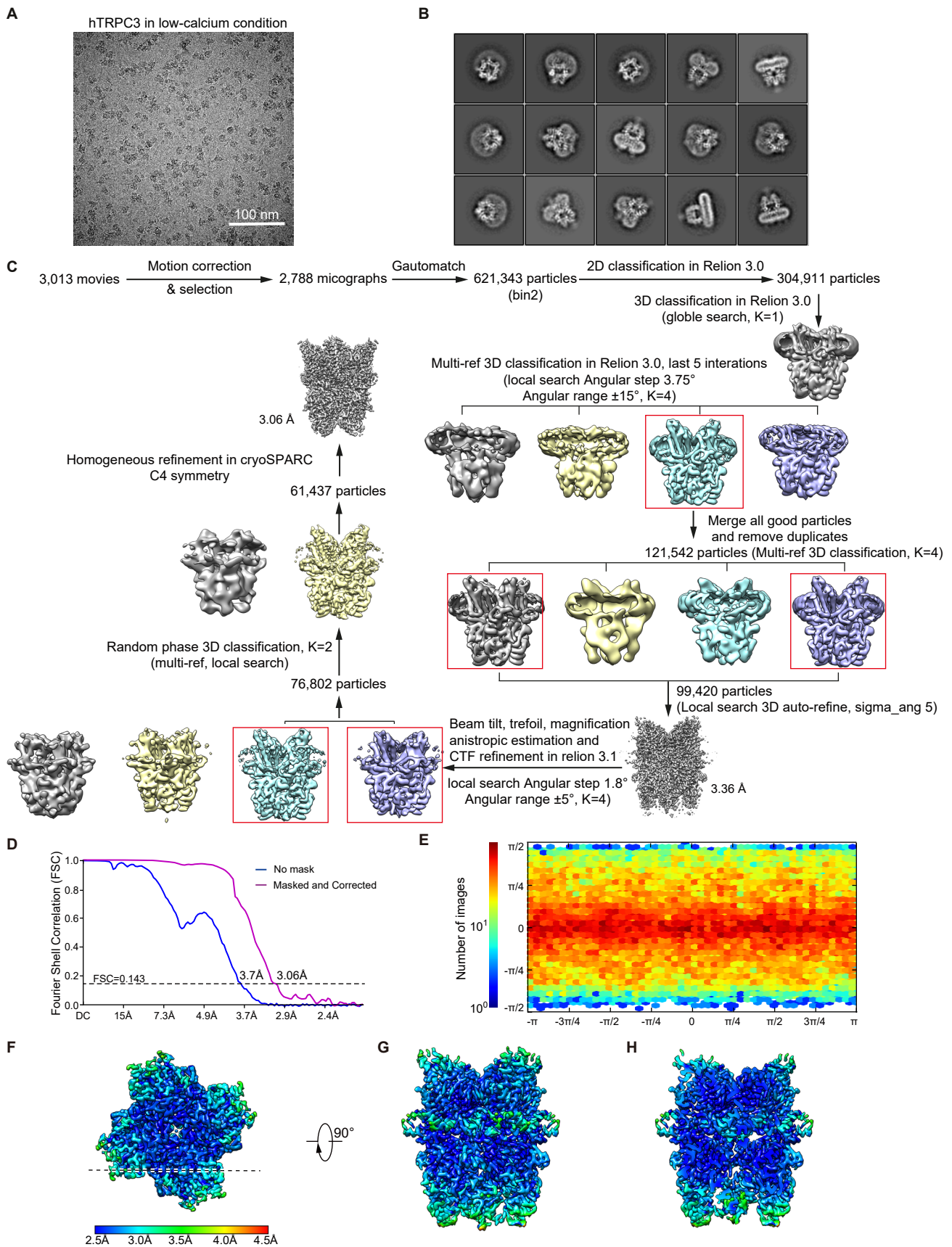


Figure S3 | Cryo-EM image analysis of hTRPC3 in the low-calcium state. Related to Figure 1.

(A) Representative raw micrograph of hTRPC3 in the low-calcium state.

(B) Representative 2D class average of hTRPC3 in the low-calcium state.

(C) Flowchart of hTRPC3 in the low-calcium state by cryo-EM data processing.

(D) FSC curves of final refinement for hTRPC3 in the low-calcium state (C4 symmetry) after correcting for masking effects. Resolution estimations were based on the criterion of the FSC 0.143 cutoff.

(E) Angular distribution of final refinement for hTRPC3 in the low-calcium state. This is a standard output from cryoSPARC.

(F) Top view of local resolution estimation of hTRPC3 in the low-calcium state.

(G) Side view of local resolution estimation of hTRPC3 in the low-calcium state.

(H) The cross-section of local resolution estimation of hTRPC3 in the low-calcium state. The position of the cross-section is indicated by a dashed line in (F).

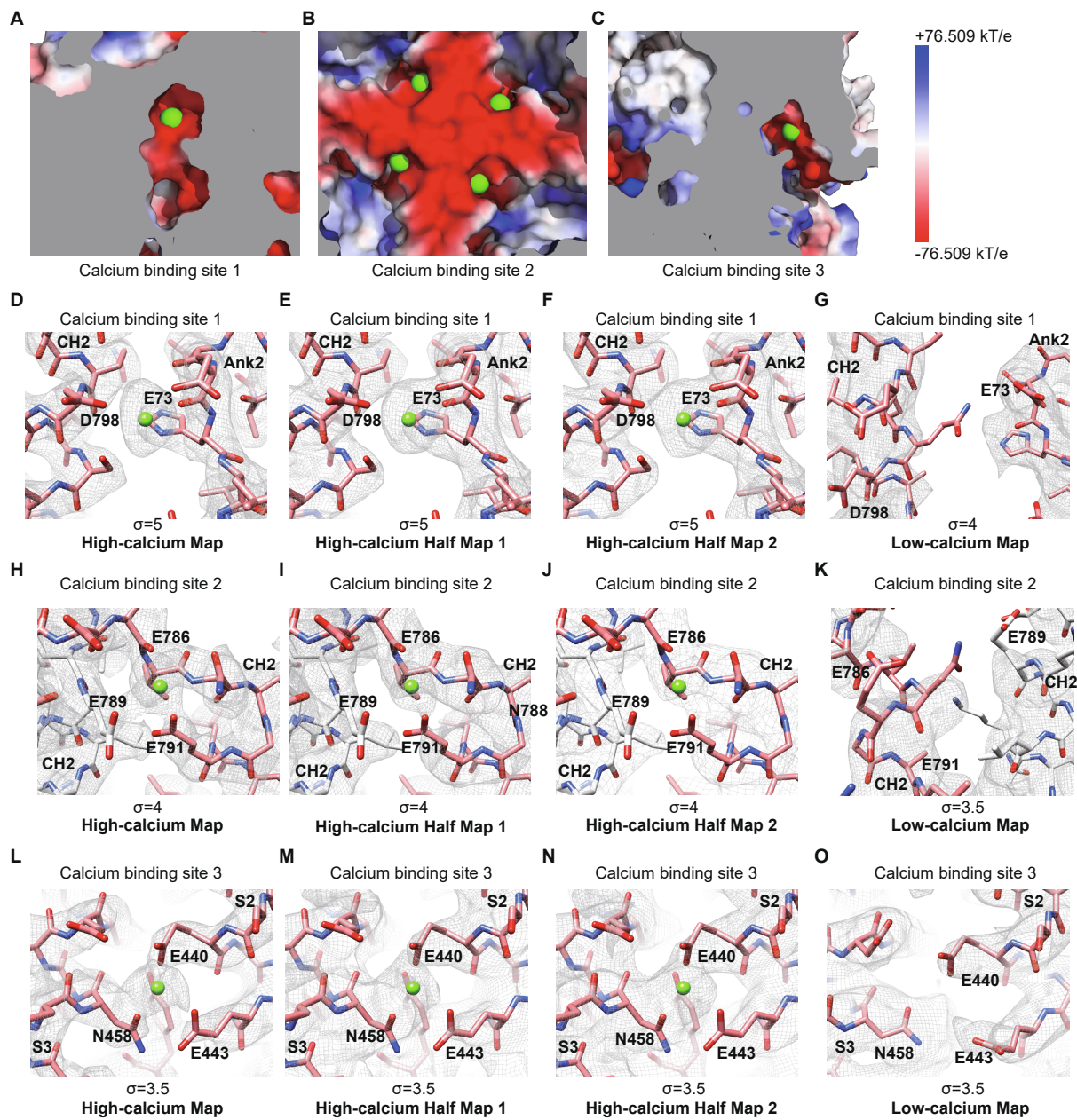


Figure S4 | Three calcium-binding sites in hTRPC3. Related to Figure 2.

(A-C) The electrostatic potential of calcium-binding site 1-3 calculated by PyMOL. The calcium ions are represented as green spheres.

(D) Close-up view of the calcium-binding site 1 in the final reconstruction of hTRPC3 in the high-calcium state. Densities of ion and its surrounding amino acids are presented as grey mesh and contoured at 5σ .

(E-F) Close-up view of the calcium-binding site 1 in two half maps of hTRPC3 in the high-calcium state. The densities of ion and its surrounding amino acids are presented as grey mesh and contoured at 5σ .

(G) Close-up view of the calcium-binding site 1 in the final reconstruction of hTRPC3 in the low-calcium state. The densities of ion and its surrounding amino acids are presented as grey mesh and contoured at 4σ .

(H) Close-up view of the calcium-binding site 2 of the final reconstruction of hTRPC3 in the high-calcium state. The densities of ion and its surrounding amino acids are presented as grey mesh and contoured at 4σ .

(I-J) Close-up view of the calcium-binding site 2 in two half maps of hTRPC3 in the high-calcium state. The densities of ion and its surrounding amino acids are presented as grey mesh and contoured at 4σ .

(K) Close-up view of the calcium-binding site 2 of the final reconstruction of hTRPC3 in the low-calcium state. The densities of ion and its surrounding amino acids are presented as grey mesh and contoured at 3.5σ .

(L) Close-up view of the calcium-binding site 3 of the final reconstruction of hTRPC3 in the high-calcium state. The densities of ion and its surrounding amino acids are presented as grey mesh and contoured at 3.5σ .

(M-N) Close-up view of the calcium-binding site 3 in two half maps of hTRPC3 in the high-calcium state. The densities of ion and its surrounding amino acids are presented as grey mesh and contoured at 3.5σ .

(O) Close-up view of the calcium-binding site 3 of the final reconstruction of hTRPC3 in the low-calcium state. The densities of ion and its surrounding amino acids are presented as grey mesh and contoured at 3.5σ .

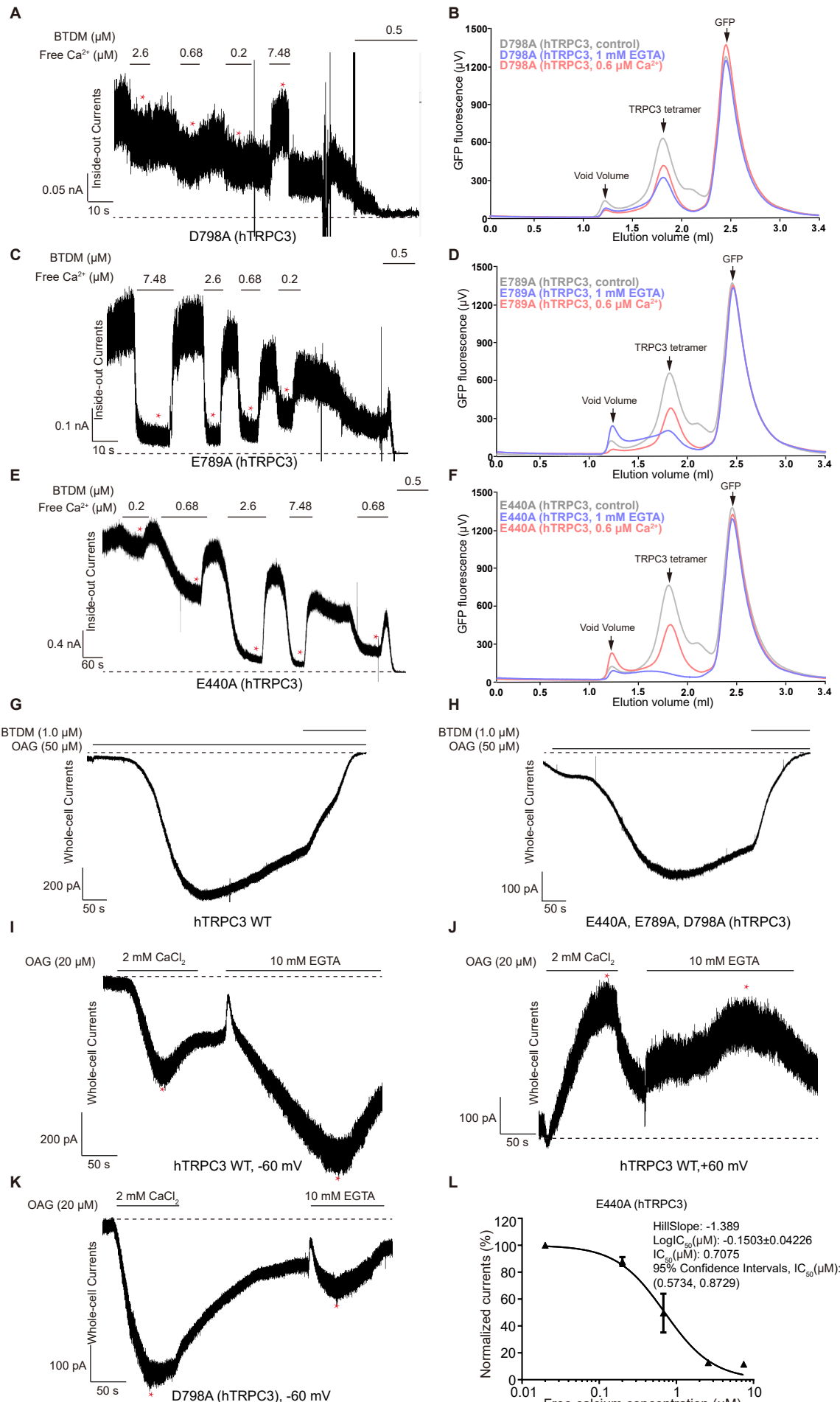


Figure S5 | Calcium regulation of hTRPC3. Related to Figure 2.

(A) Macroscopic currents of hTRPC3 D798A mutant recorded in the inside-out mode. Zero current is indicated by a dashed line. The currents used for quantification are labeled by asterisks. (B) Representative FSEC profile of the cell lysates of hTRPC3 D798A mutant after heat treatment at 48°C for 10 min with or without 0.6 μM calcium. (C) Macroscopic currents of hTRPC3 mutation E789A recorded in the inside-out mode. Zero current is marked as a dashed line. The currents used for quantification are labeled by asterisks. (D) Representative FSEC profile of the cell lysates of hTRPC3 E789A mutant after heat treatment at 48°C for 10 min with or without 0.6 μM calcium. (E) Macroscopic currents of hTRPC3 E440A mutant recorded in the inside-out mode. Zero current is indicated by a dashed line. The currents used for quantification are labeled by asterisks. (F) Representative FSEC profile of the cell lysates of hTRPC3 E440A mutant recorded in the inside-out mode. Zero current is indicated by a dashed line. The currents used for quantification are labeled by asterisks. (G-H) Macroscopic currents of wild-type hTRPC3 and E440A, E789A, D798A mutant recorded in whole-cell mode and activated by OAG and inhibited by BTDM. Zero current is labeled as a dashed line. (I-J) Macroscopic currents of wild-type hTRPC3 recorded in whole-cell mode. Cells were activated by OAG in high calcium solution (2 mM Ca^{2+}) and then by OAG in low calcium solution (10 mM EGTA) with the holding potential at -60 mV and +60 mV. Zero current is labeled as a dashed line. The peak currents used for calculations are labeled by asterisks. (K) Macroscopic currents of D798A mutant recorded in whole-cell mode and activated by OAG in high calcium solution (2 mM Ca^{2+}) and then by OAG in low calcium solution (10 mM EGTA) at -60 mV. The peak currents used for calculations are labeled by asterisks. (L) Dose-response curve for calcium inhibition of hTRPC3 CBS3 mutation E440A overexpressed in HEK293F cells. Data are shown as mean \pm SD, n=3.

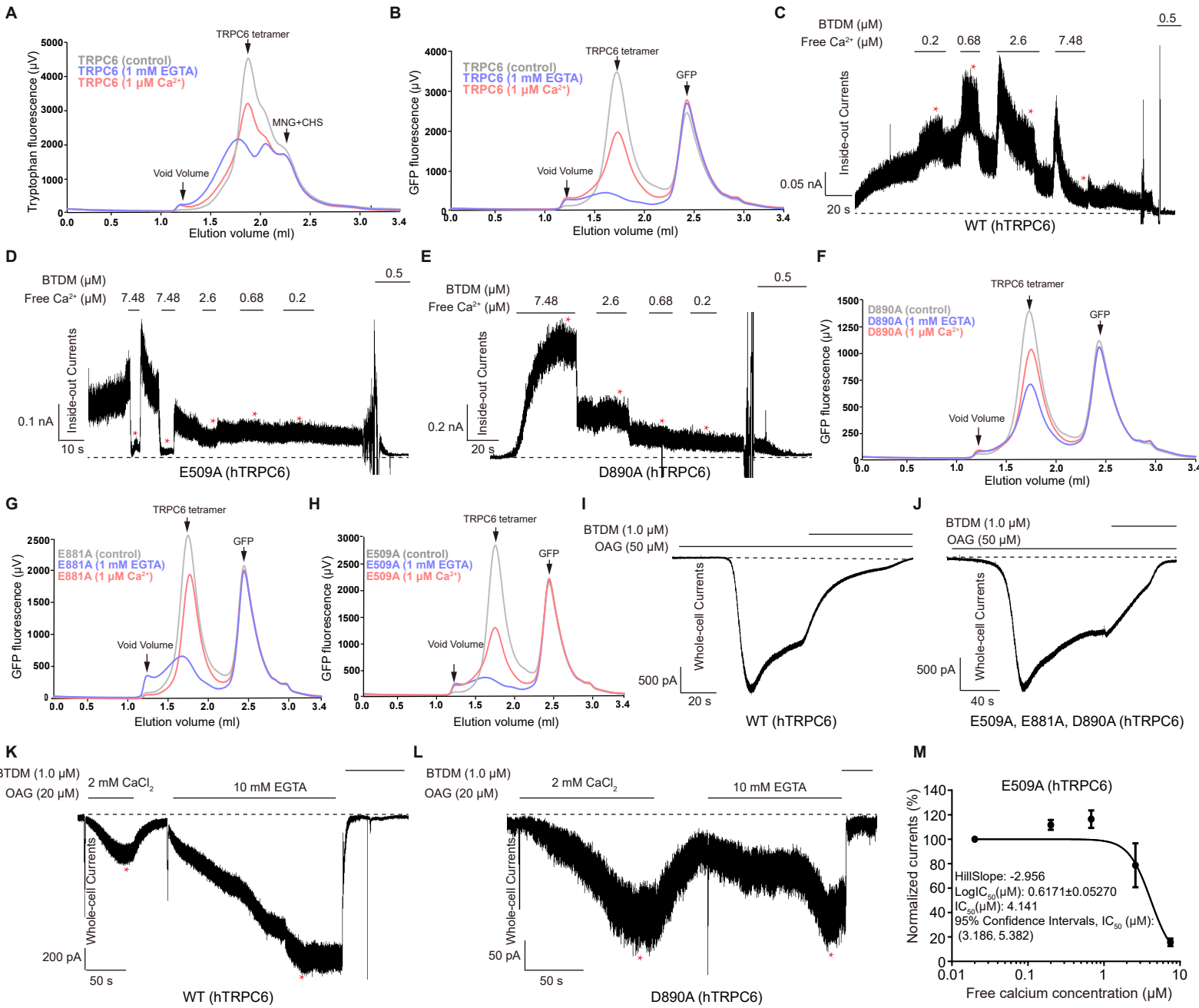


Figure S6 | Calcium regulation of hTRPC6. Related to Figure 4.

- (A) Representative FSEC profile of purified hTRPC6 after heat treatment at 43°C for 10 min with or without 1 μ M calcium.
- (B) Representative FSEC profile of wild-type hTRPC6 cell lysates after heat treatment at 46°C for 10 min with or without 1 μ M calcium.
- (C-E) Macroscopic currents of wild-type hTRPC6, E509A, and D890A mutants recorded in inside-out mode. The zero current is indicated by a dashed line in the raw trace. The currents used for quantifications are labeled by asterisks.
- (F-H) Representative FSEC profile of cell lysates of hTRPC6 D890A, E881A, and E509A mutants after heat treatment at 46°C for 10 min with or without 1 μ M calcium.
- (I-J) Macroscopic currents of wild-type hTRPC6 and E509A, E881A, D890A triple mutant recorded in whole-cell mode and activated by OAG and inhibited by BTDM. The zero current is marked as a dashed line in the raw trace.
- (K-L) Macroscopic currents of wild-type hTRPC6 and D890A mutant recorded in whole-cell mode and activated by OAG in high calcium solution (2 mM Ca^{2+}) and then by OAG in low calcium solution (10 mM EGTA) at -60 mV. The zero current is indicated by a dashed line in the raw trace. The peak currents used for calculations are labeled by asterisks.
- (M) Dose-response curve for calcium inhibition of hTRPC6 CBS3 mutation E509A overexpressed in HEK293F cells. Data are shown as mean \pm SD, n=3.

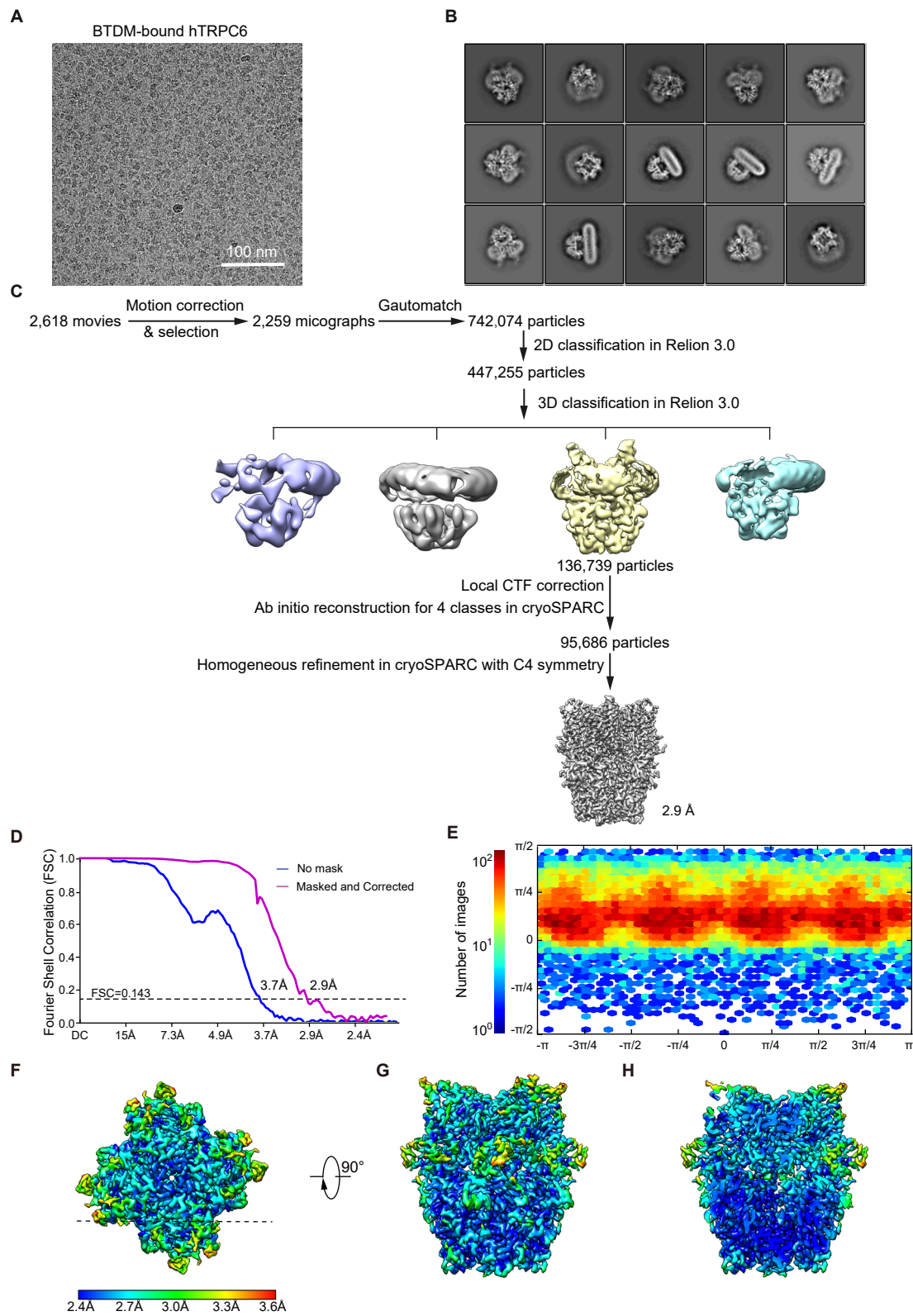


Figure S7 | Cryo-EM image analysis of BTDM-bound hTRPC6. Related to Figure 4.

- (A) Representative raw micrograph of BTDM-bound hTRPC6.
- (B) Representative 2D class average of BTDM-bound hTRPC6.
- (C) Flowchart of BTDM-bound hTRPC6 cryo-EM data processing.
- (D) FSC curves of final refinement for BTDM-bound hTRPC6 in the high-calcium state (C4 symmetry) after correction for masking effects. Resolution estimations were based on the criterion of the FSC 0.143 cutoff.
- (E) Angular distribution of final refinement for BTDM-bound hTRPC6 in the high-calcium state. This is a standard output from cryoSPARC.
- (F) Local resolution estimation of BTDM-bound hTRPC6 in the high-calcium state in top view.
- (G) Side view of local resolution estimation of BTDM-bound hTRPC6.
- (H) The cross-section of local resolution estimation of BTDM-bound hTRPC6. The position of the cross-section was indicated as a dashed line in (F).

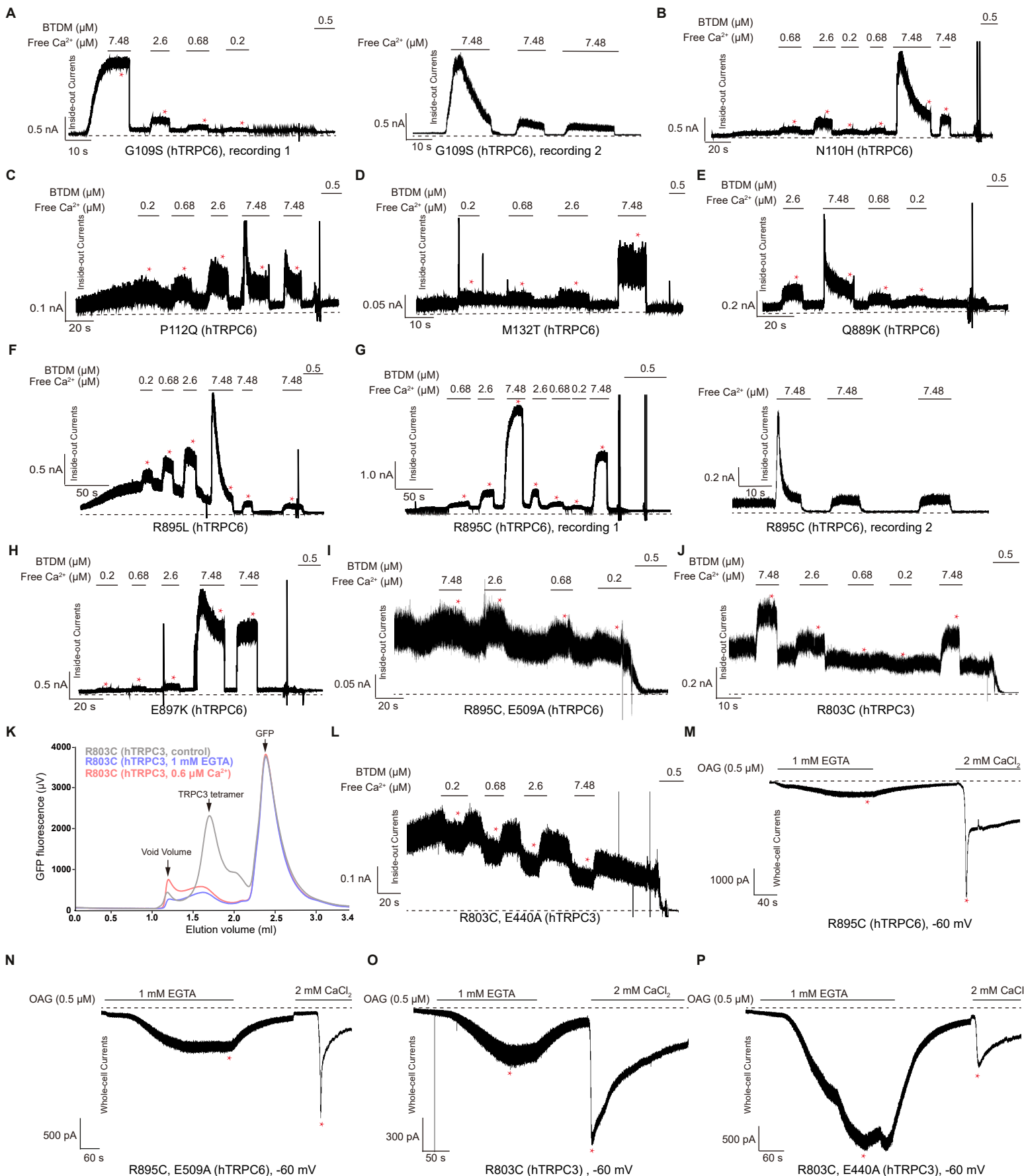


Figure S8 | Calcium regulation of gain-of-function FSGS mutants of hTRPC6. Related to Figure 5.

(A-H) Macroscopic currents of hTRPC6 gain-of-function FSGS mutants: G109S, N110H, P112Q, M132T, Q889K, R895L, R895C, and E897K recorded in the inside-out mode.

(I) Macroscopic currents of R895C, E509A hTRPC6 mutant recorded in the inside-out mode.

(J) Macroscopic currents of hTRPC3 gain-of-function mutant R803C recorded in the inside-out mode.

(K) Representative FSEC profile of cell lysates of hTRPC3 gain-of-function mutant R803C after heat treatment at 45°C for 10 min with or without 0.6 μM calcium.

(L) Macroscopic currents of hTRPC3 R803C, E440A mutant recorded in the inside-out mode.

(M-N) Whole-cell currents of hTRPC6 R895C and R895C, E509A mutant are activated by OAG in low calcium solution (1 mM EGTA) and then by OAG in high calcium solution (2 mM Ca^{2+}) at -60 mV.

(O-P) Whole-cell currents of hTRPC3 R803C and R803C, E440A mutant are activated by OAG in low calcium solution (1 mM EGTA) and then by OAG in high calcium solution (2 mM Ca^{2+}) at -60 mV. In all the electrophysiology traces, the zero current is indicated as a dashed line. The currents used for calculations are labeled by asterisks.

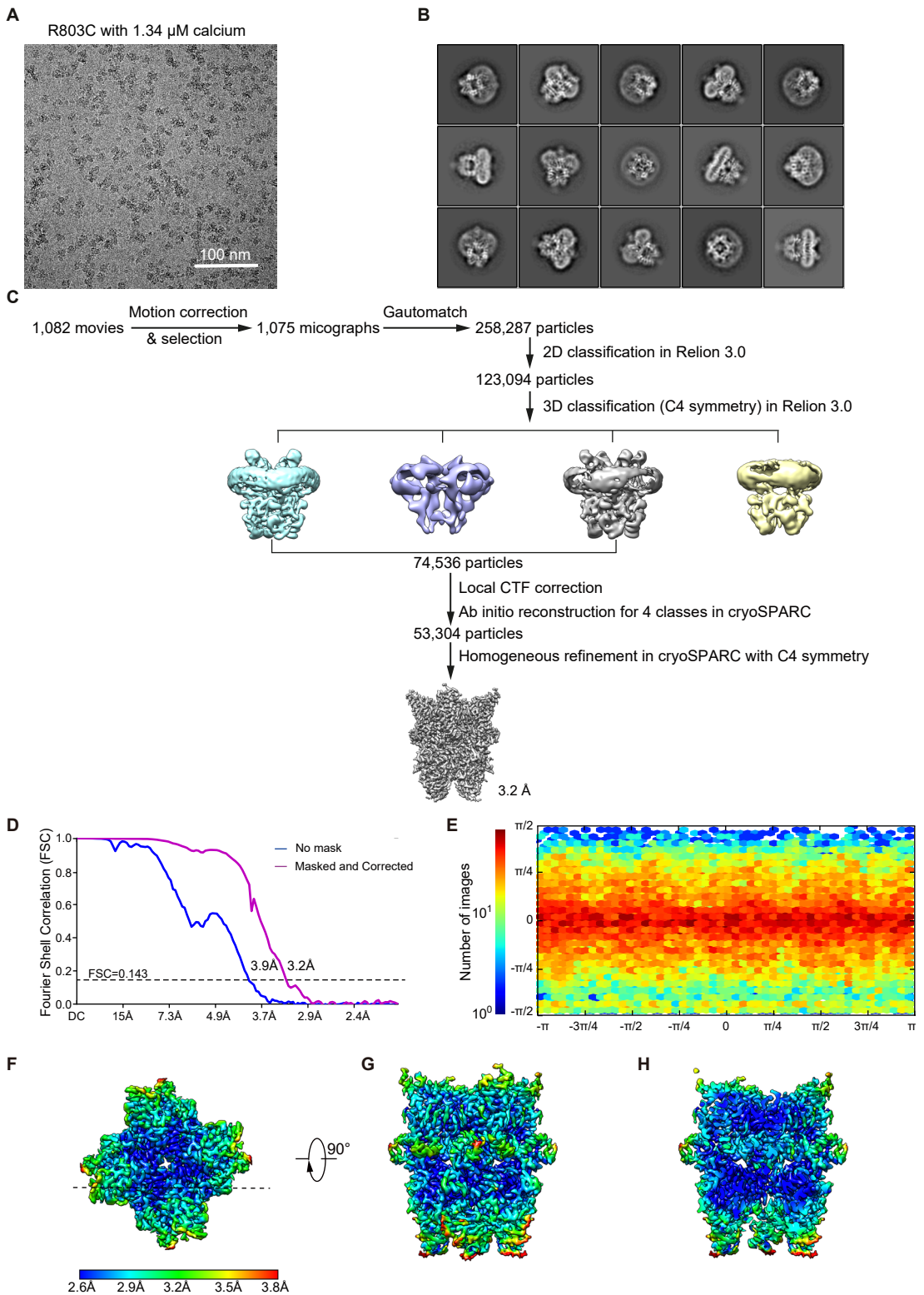


Figure S9 | Cryo-EM image analysis of hTRPC3 R803C mutant in the presence of 1.34 μM calcium. Related to Figure 6.

- (A) Representative raw micrograph of hTRPC3 R803C mutant with 1.34 μM calcium.
- (B) Representative 2D class average of hTRPC3 R803C mutant with 1.34 μM calcium.
- (C) Flowchart of hTRPC3 R803C mutant with 1.34 μM calcium cryo-EM data processing.
- (D) FSC curves of final refinement for hTRPC3 R803C mutant in the presence of 1.34 μM calcium (C4 symmetry) after correction for masking effects. Resolution estimations were based on the criterion of the FSC 0.143 cutoff.
- (E) Angular distribution of final refinement for hTRPC3 R803C mutant with 1.34 μM calcium. This is a standard output from cryoSPARC.
- (F) Local resolution estimation of hTRPC3 R803C mutant with 1.34 μM calcium in top view.
- (G) Side view of local resolution estimation of hTRPC3 R803C mutant with 1.34 μM calcium.
- (H) The cross-section of local resolution estimation of hTRPC3 R803C mutant with 1.34 μM calcium. The position of the cross-section was indicated as a dashed line in (F).

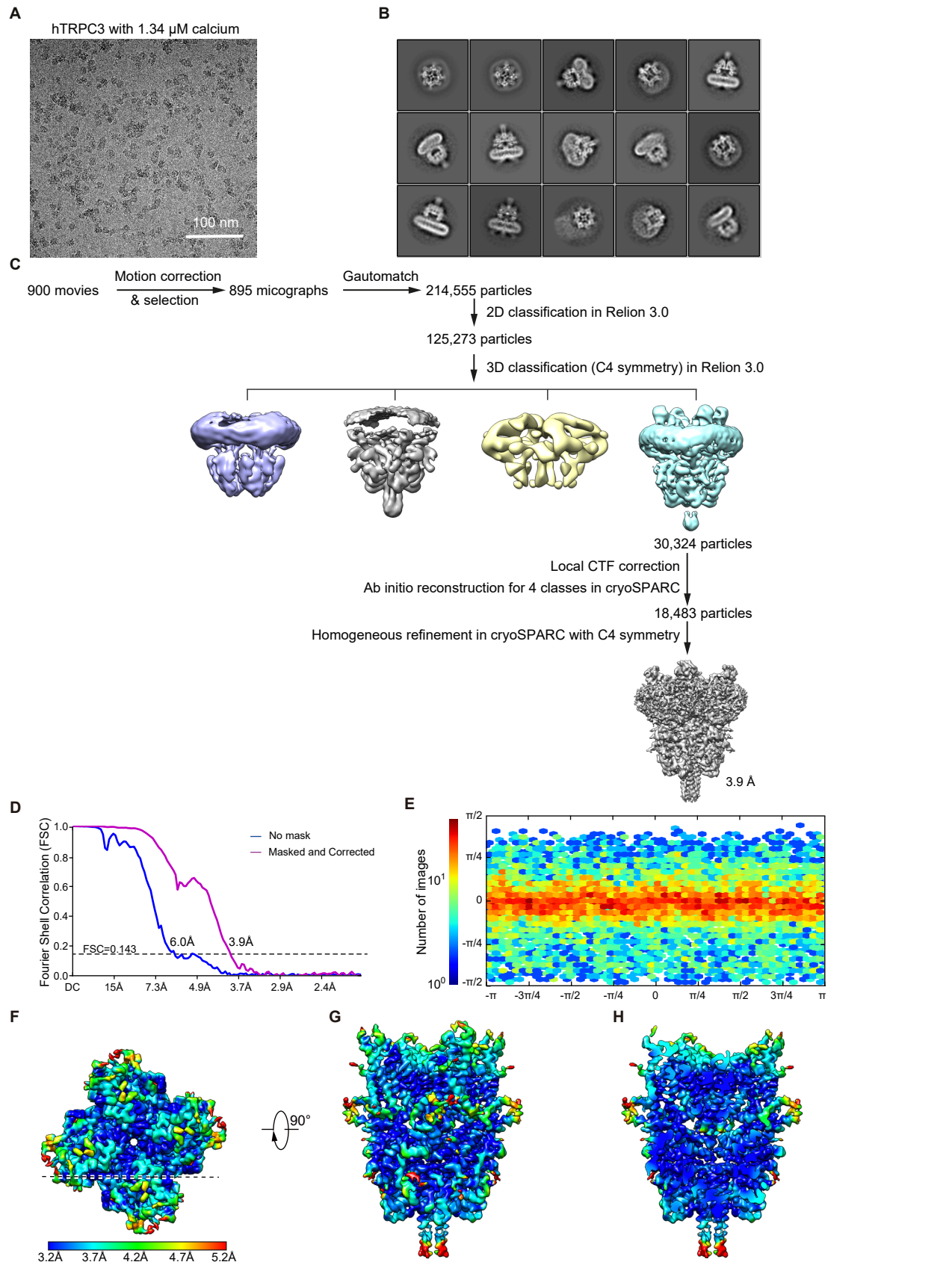


Figure S10 | Cryo-EM image analysis of wild type hTRPC3 with 1.34 μM calcium. Related to Figure 6.

- (A) Representative raw micrograph of wild type hTRPC3 with 1.34 μM calcium.
- (B) Representative 2D class average of wild type hTRPC3 with 1.34 μM calcium.
- (C) Flowchart of wild-type hTRPC3 with 1.34 μM calcium cryo-EM data processing.
- (D) FSC curves of final refinement for wild-type hTRPC3 with 1.34 μM calcium (C4 symmetry) after correction for masking effects. Resolution estimations were based on the criterion of the FSC 0.143 cutoff.
- (E) Angular distribution of final refinement for wild-type hTRPC3 with 1.34 μM calcium. This is a standard output from cryoSPARC.
- (F) Local resolution estimation of wild type hTRPC3 with 1.34 μM calcium in top view.
- (G) Side view of local resolution estimation of wild type hTRPC3 with 1.34 μM calcium.
- (H) The cross-section of local resolution estimation of wild type hTRPC3 with 1.34 μM calcium. The position of the cross-section was indicated as a dashed line in (F).

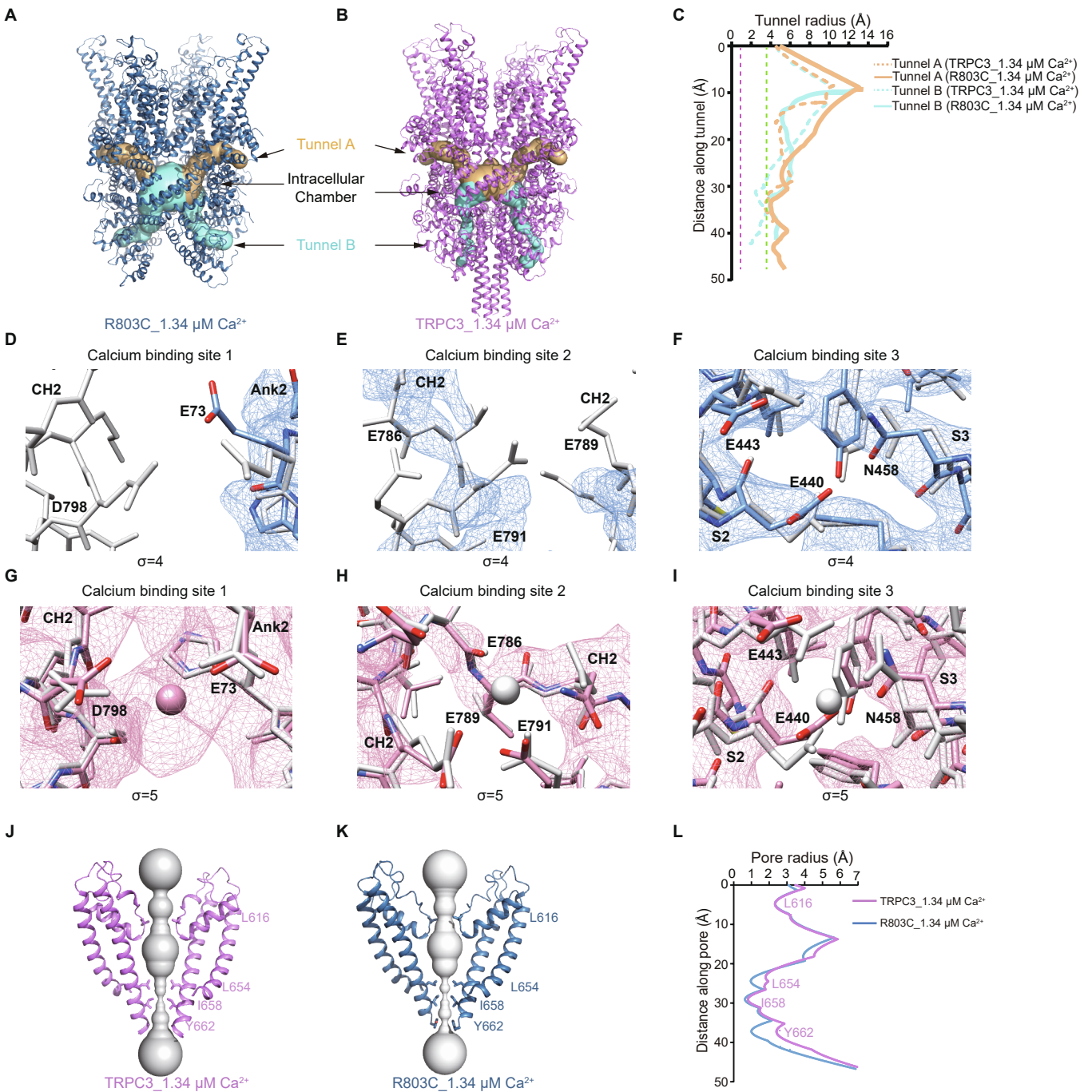


Figure S11 | Three calcium-binding sites in hTRPC3 and hTRPC3 mutant R803C with 1.34 μM calcium. Related to Figure 6.

(A-B) The putative ion permeation pathways between the intracellular chamber of ICD and cytosol of wild type TRPC3 and R803C mutant in the presence of 1.34 μM calcium were calculated by Caver. The structures are colored in blue (hTRPC3 R803C mutant) and pink (wild type hTRPC3), respectively.

(C) Calculated tunnel radius shown in (A) and (B). The radius of dehydrated calcium is labeled as a pink dashed line and fully hydrated calcium is labeled as a green dashed line.

(D-F) Close-up views of the calcium-binding sites 1-3 in the sharpened map of hTRPC3 mutant R803C in the presence of 1.34 μM calcium. The densities of ions and their surrounding amino acids are contoured at 4 σ . The electron densities and atomic models of R803C are colored in blue and the aligned models of wild type hTRPC3 in a low-calcium state are colored in grey for comparison.

(G-I) Close-up view of the CBS1-3 in the final reconstruction of wild-type hTRPC3 with 1.34 μM calcium. The densities of ions and their surrounding amino acids are contoured at 5 σ . The map densities and models of hTRPC3 with 1.34 μM calcium are colored in pink and the aligned models of hTRPC3 in the high-calcium state are colored in grey for comparison.

(J-K) Side view of the S5-S6 pore region of hTRPC3 and R803C in the presence of 1.34 μM calcium. Proteins are shown as cartoons and colored in pink and blue, respectively. The ion permeation pathways along the pore are shown as grey spheres.

(L) Pore profiles of hTRPC3 and R803C mutant with 1.34 μM calcium calculated using HOLE.

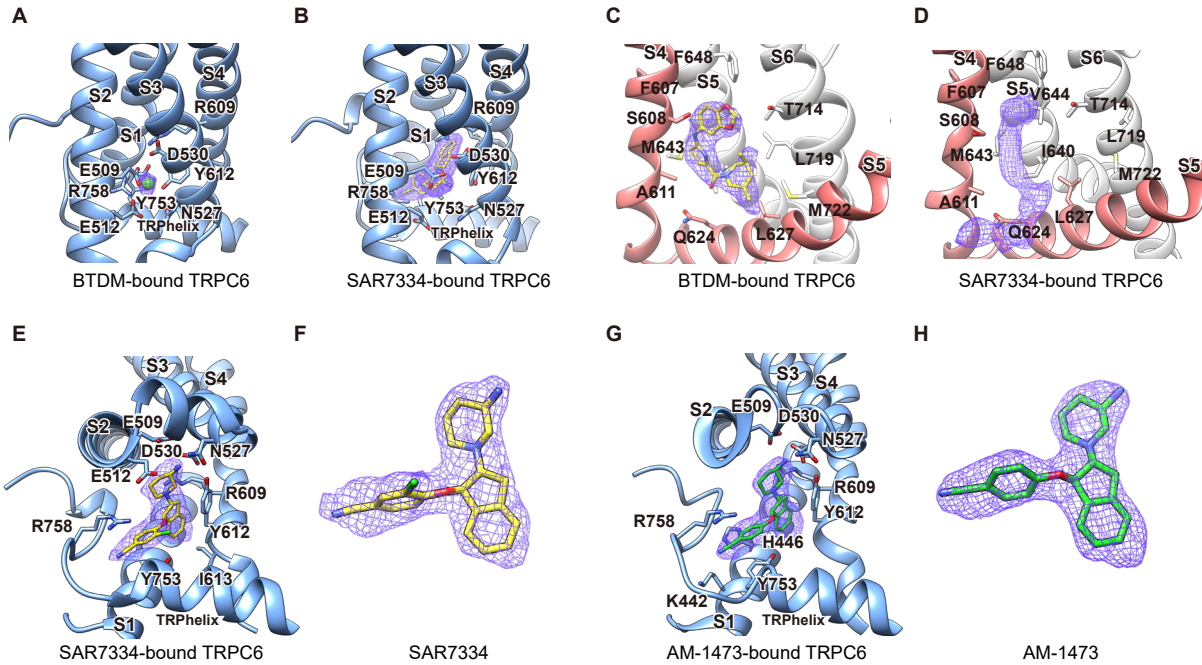


Figure S12 | Inhibitor-binding sites in hTRPC6. Related to Figure 7.

(A) Corresponding SAR7334 binding pocket in BTDM-bound hTRPC6. Subunit A is shown as a cartoon and colored in blue. Residues related to SAR7334 binding are shown as sticks. The corresponding calcium density is shown as purple mesh. The modeled calcium is shown as a green sphere.

(B) SAR7334 binding pocket in SAR7334-bound hTRPC6. SAR7334 is presented as sticks with purple mesh. Related residues are presented as sticks.

(C) BTDM binding pocket in hTRPC6. Subunit A and adjacent subunit D are indicated in pink and gray, respectively. BTDM is shown as yellow sticks. Densities of BTDM and interacting residues are contoured at 4σ and BTDM is shown as purple mesh.

(D) Corresponding BTDM binding pocket in SAR-bound hTRPC6 map. Residues related to BTDM binding are presented as sticks. The extra unknown density is shown as purple mesh.

(E) Close-up view of SAR7334 binding pocket shown from the bottom view.

(F) Structure of SAR7334 with density shown in purple mesh.

(G) AM-1473 binding pocket in AM-1473-bound hTRPC6 shown from the bottom view. AM-1473 is shown in green sticks with purple mesh and related residues are presented as sticks.

(H) Structure of AM-1473 with density shown in purple mesh.

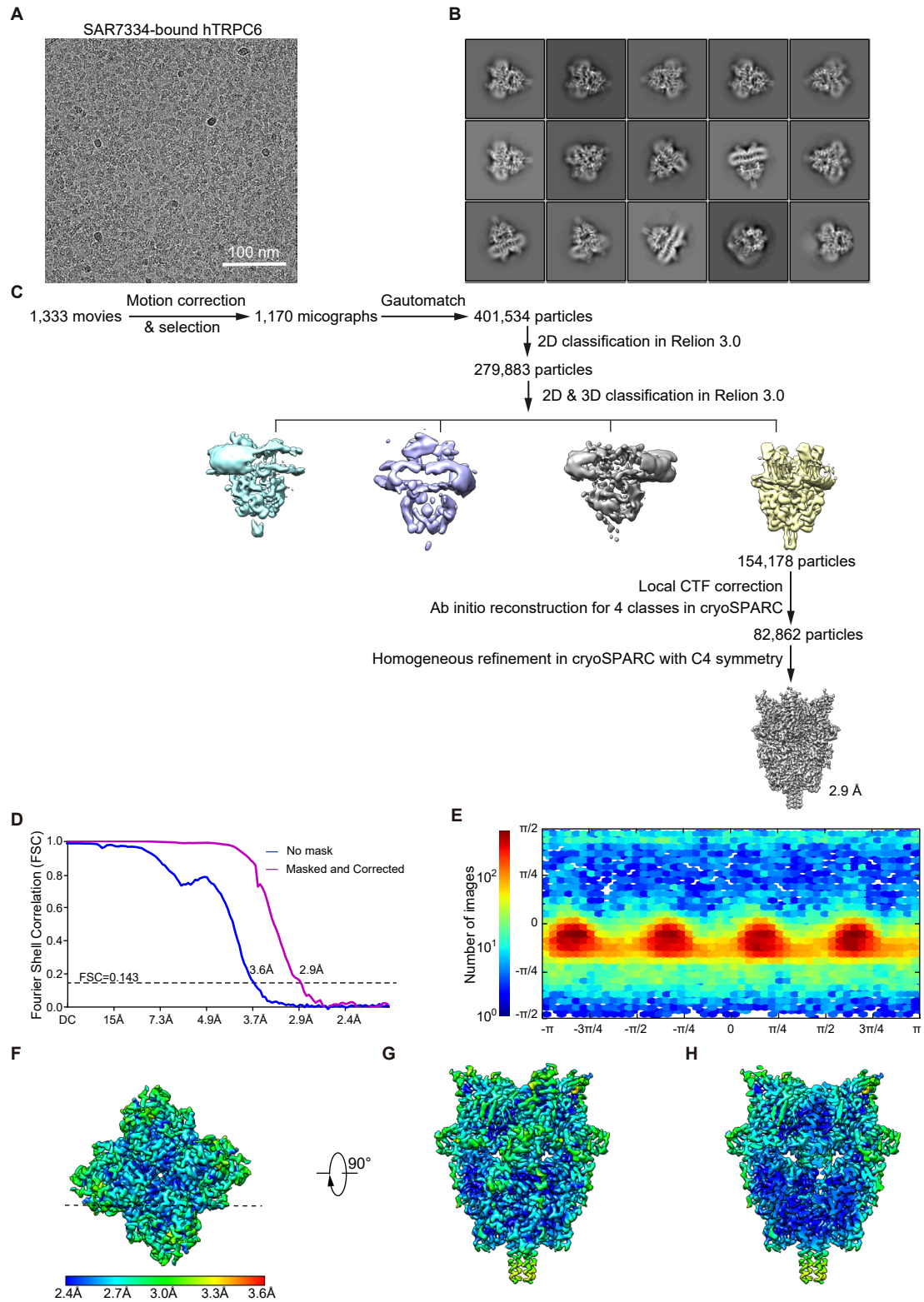


Figure S13 | Cryo-EM image analysis of SAR7334-bound hTRPC6. Related to Figure 7.

- (A) Representative raw micrograph of SAR7334-bound hTRPC6.
- (B) Representative 2D class average of SAR7334-bound hTRPC6.
- (C) Flowchart of SAR7334-bound hTRPC6 cryo-EM data processing.
- (D) FSC curves of final refinement for SAR7334-bound hTRPC6 (C4 symmetry) after correction for masking effects. Resolution estimations were based on the criterion of the FSC 0.143 cutoff.
- (E) Angular distribution of final refinement for SAR7334-bound hTRPC6. This is a standard output from cryoSPARC.
- (F) Local resolution estimation of SAR7334-bound hTRPC6 in top view.
- (G) Side view of local resolution estimation of SAR7334-bound hTRPC6.
- (H) The cross-section of local resolution estimation of SAR7334-bound hTRPC6. The position of the cross-section was indicated as a dashed line in (F).

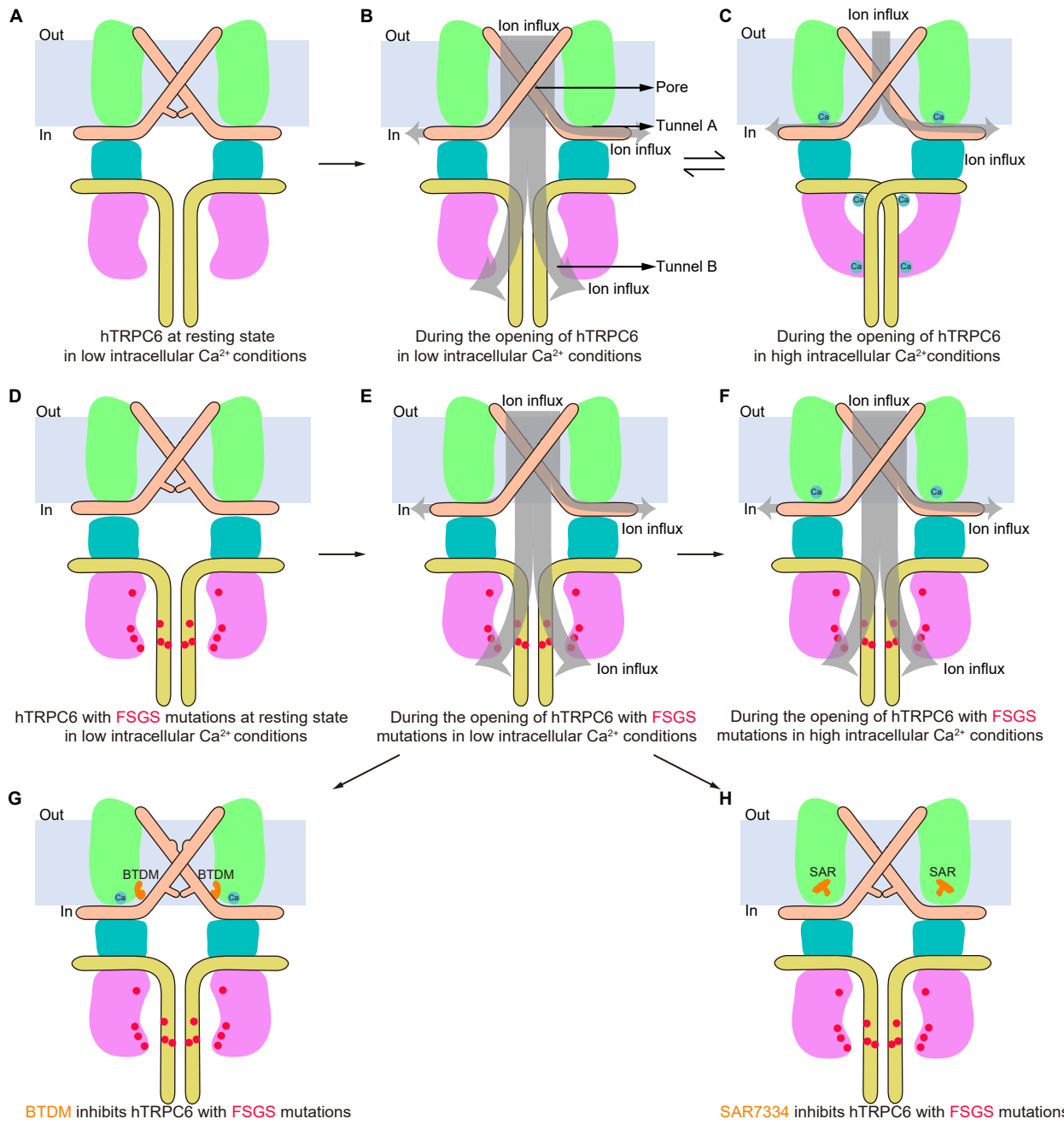


Figure S14 | Model for calcium regulation of hTRPC3/6/7 channels, exemplified by hTRPC6. Related to Figure 7.

(A) Side view of hTRPC6 channel in low-calcium resting state shown as a cartoon. Each domain is colored differently, the ARD in pink, LHD in blue, VSLD in green, pore helices in orange, and C terminal helices in yellow. The resting state mimics the loosely packed state.

(B) During the basal opening of hTRPC6 in low intracellular calcium concentration. Ion influx is indicated by gray bars.

(C) During the basal opening of hTRPC6 in high intracellular calcium concentration. Ion influx is indicated by gray bars. Calcium ions are represented as cyan spheres. In the presence of elevated cytosolic calcium concentration, the calcium ions can bind to both inhibitory and activating calcium-binding site. hTRPC6 adopts tightly packed structure with restricted ion flow in ICD.

(D) Side view of hTRPC6 channel with FSGS mutations in resting state shown as a cartoon model. Each domain is colored the same as in (A). The FSGS mutations are marked as red dots.

(E) During the basal opening of hTRPC6 with FSGS mutations in low intracellular calcium concentration.

(F) During the basal opening of hTRPC6 with FSGS mutations in high intracellular calcium concentration, with unrestricted ion flow in ICD.

(G) The inhibited state of hTRPC6 channel with FSGS mutations with BTDM binding.

(H) The inhibited state of hTRPC6 channel with FSGS mutations with SAR7334 binding.

Table. S1 Cryo-EM data collection, refinement and validation statistics. Related to Figures 1, 4, 6 and 7.

	hTRPC3 High [Ca ²⁺] 7DXB EMD-30903	hTRPC3 Low [Ca ²⁺] 7DXC EMD-30904	hTRPC3 1.34μM Ca ²⁺ 7DXD EMD-30905	hTRPC3 R803C 1.34μM Ca ²⁺ 7DXE EMD-30906	hTRPC6 BTDM 7DXF EMD-30907	hTRPC6 SAR7334 7DXG EMD-30908
Data collection and processing						
Magnification	130,000 ×	130,000 ×	130,000 ×	130,000 ×	130,000 ×	130,000 ×
Voltage (kV)	300	300	300	300	300	300
Electron exposure (e ⁻ /Å ²)	48	48	48	48	48	48
Defocus range (μm)	-1.5 to -2.0	-1.5 to -2.0	-1.5 to -2.0	-1.5 to -2.0	-1.5 to -2.0	-1.5 to -2.0
Pixel size (Å)	1.045	1.045	1.045	1.045	1.045	1.045
Symmetry imposed	C4	C4	C4	C4	C4	C4
Initial particle images (no.)	329,549	621,343	214,555	258,287	742,074	401,534
Final particle images (no.)	35,441	61,437	18,483	53,304	95,686	82,862
Map resolution (Å)	2.7	3.1	3.9	3.2	2.9	2.9
FSC threshold	0.143	0.143	0.143	0.143	0.143	0.143
Map resolution range (Å)	250.0-2.7	250.0-3.1	250.0-3.9	250.0-3.2	250.0-2.9	250.0-2.9
Refinement						
Initial model used (PDB code)	5ZBG	6CUD	5ZBG	6CUD	5YX9	5YX9
Model resolution (Å)	2.7	3.1	3.9	3.2	2.9	2.9
FSC threshold	0.143	0.143	0.143	0.143	0.143	0.143
Model resolution range (Å)	250.0-2.7	250.0-3.1	250.0-3.9	250.0-3.2	250.0-2.9	250.0-2.9
Map sharpening B factor (Å ²)	-101.9	-113.0	-105.6	-116.5	-128.4	-148.2
Model composition						
Non-hydrogen atoms	24,244	22,896	23,628	22,280	22,940	23,432
Protein residues	2,952	2,808	2,928	2,740	2,740	2,796
Ligands	32	20	12	20	40	36
B factors (Å ²)						
Protein	37.07	198.16	111.13	159.78	110.93	112.21
Ligand	46.64	205.80	102.94	164.09	122.38	134.78
R.m.s. deviations						
Bond lengths (Å)	0.004	0.004	0.004	0.004	0.004	0.004
Bond angles (°)	0.955	0.929	0.966	1.023	1.074	1.015
Validation						
MolProbity score	1.81	2.12	1.62	1.55	2.06	1.89
Clashscore	5.18	8.71	7.33	8.11	7.43	7.78
Poor rotamers (%)	2.34	4.88	1.25	0.35	3.38	3.01
Ramachandran plot						
Favored (%)	96.30	97.33	97.22	97.48	96.30	97.52
Allowed (%)	3.70	2.53	2.78	2.37	3.56	2.48
Disallowed (%)	0.00	0.14	0.00	0.15	0.15	0.00